An integrated sedimentological-chemostratigraphic study of the Late Devonian-Early Mississipian Chattanooga Formation in Kansas: high-resolution stratigraphy and organic matter accumulation

by

Spencer C. Brower

B.S., Grand Valley State University, 2017

A THESIS

submitted in partial fulfillment of the requirements for the degree

MASTER OF SCIENCE

Department of Geology
College of Arts and Sciences

KANSAS STATE UNIVERSITY
Manhattan, Kansas

2019

Approved by:

Major Professor
Dr. Karin Goldberg

Copyright

Abstract

The Chattanooga (Woodford) Formation is an organic-rich, black shale that was deposited in Kansas and Oklahoma during the late Devonian and the upper part of the early Mississippian as a result of a transgressive sequence. It is both a source rock and unconventional hydrocarbon reservoir. This research aimed to produce a high-resolution, sequence stratigraphic framework based on the identification of key stratigraphic surfaces, systems tracts and depositional sequences. The framework was used to infer the processes that controlled sediment accumulation and produced this mudrock succession. The analyses included a centimeter to millimeter scale sedimentological description, aided by petrography and XRD, and the generation of chemostratigraphic profiles using hand-held XRF (HHXRF) point data. A smaller sample set was analyzed using inductively-coupled plasma mass spectrometry (ICP-MS) and LECO carbon/sulfur analyzer. Facies descriptions and HHXRF data were collected by analyzing a core from Douglas County, Kansas. Chemostratigraphic data were used to detect variations in the concentration of specific elements that can provide information on sediment source at the time of deposition, primary productivity and bottom-water oxygen concentrations (anoxic vs. oxygenated). Three depositional sequences, characterized by distinct facies associations and chemostratigraphic signatures, were identified in the studied succession. This study on the Chattanooga (Woodford) Formation suggests that the main control in the accumulation of organic matter was primary productivity. In most instances, anoxia seems to have been driven by the high organic flux. The most favorable conditions for the formation of organic-rich sediments seems to be when high organic flux is accompanied by anoxia (due to increasing water depth), such as recorded in Sequence 3.

Table of Contents

List of Figures

List of Tables

Acknowledgements

I would first like to thank Dr. Goldberg for her support and patience throughout my learning experience at Kansas State University. I could not have asked for a better advisor. I'd also like to thank Dr. Kempton and Dr. Ghanbarian for their input on the project and for being on my committee. Thank you to Dr. Lacroix and my fellow graduate student Creenen Mcguire for all of their help in regards to the XRD data. This research was made possible by the funding received from the AAPG Grants-in-Aid program and by the Kansas Geological Survey allowing us to work with one of their cores. Lastly, I would like to thank the remainder of the graduate students that I had the pleasure of working with and learning alongside of these past couple years. This experience wouldn't have been the same without each and every person I had the privilege of meeting here at Kansas State.

Chapter 1 - Introduction

Until recently, the study of mudrocks has typically been conducted at a scale that includes all fine-grained material as one homogeneous unit (Potter, 1980). By doing this, one loses detail of what actually took place during the time the fined-grained material was being deposited. Shales and mudrocks are a topic of interest to the oil and gas industry because of their role as source rocks and unconventional reservoirs. One of the important unconventional reservoirs, and the unit of study for this research, is the Chattanooga Formation in Kansas, equivalent to the Woodford Shale in Oklahoma and the Barnett Shale in Texas.

This research aims to uncover some of the depositional controls on the accumulation of organic material in mudrocks and shales. Previous research focused on this study area include Slatt (2012) and Turner et al. (2015, 2016). With shales being a key resource in the oil industry today for unconventional reservoirs, detailed studies of sequence stratigraphy within the Woodford/Chattanooga succession have been completed and shown correlations between stratigraphic surfaces observed in cores and outcrops with chemostratigraphy in Oklahoma (Turner et al., 2016).

Our main objectives are to: 1) establish a high-resolution sequence stratigraphic framework for the Chattanooga Formation in Kansas, 2) evaluate the physical and chemical controls on the preservation of organic material in the sediments and 3) define the allogenic mechanisms (tectonics, eustasy, sedimentary supply) controlling the sedimentary succession. Our rationale is that by identifying compositional and textural variations in the Chattanooga Formation, we can develop a sequence-stratigraphic framework and a depositional model that can potentially be applied to other shale units as a predictive tool for assessing the productive potential of the shale layer.

This study was performed on a core, API 15-045-21557, drilled in Douglas County, Kansas (Figure 1.1), containing approximately 40 feet of the Chattanooga Formation.

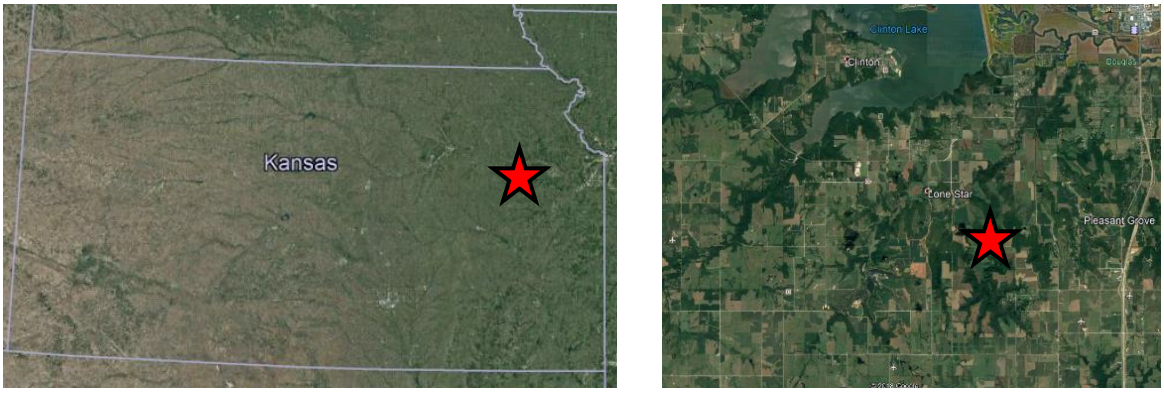

Figure 1.1 Images from Google Earth, with the red star indicating the location of the cored well in Douglas County, Kansas.

Chapter 2 - Geologic Background

The Chattanooga Formation is a dark organic-rich shale that is Late Devonian to Early Mississippian in age (Cardott et al., 2015). The Chattanooga is the name for this formation in Kansas, and a few other locations, but it is equivalent to the Woodford Shale in Oklahoma and the Barnett Shale in Texas. At the time of deposition, the paleogeographic setting of North America was very different from today (Figure 2.1). In a time of high sea level, which led to suitable conditions for accumulation of organic-rich sediment, North America was positioned at much lower latitudes and was partially covered by an epeiric sea (Woodrow et al., 1973). The deposition of this shale is unusual because most shales are deposited in calm and deep marine environments. An inland sea like the one mentioned is overall a shallower and higher energy environment that is not conducive for the accumulation of organic-

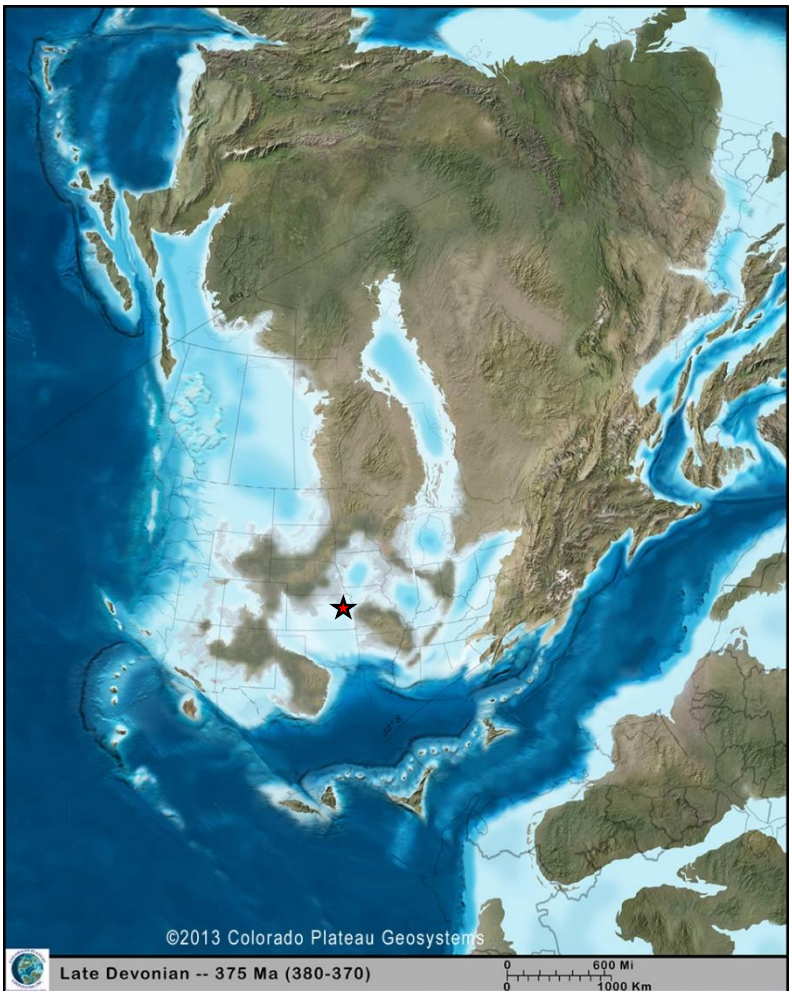

Figure 2.1 Paleogeographic reconstruction of North America overlaying a present day map of North America (Blakey, 2013). The red star indicates the approximate location of the studied core in Kansas.

rich shale (Demaison and Moore, 1980). Yet thick, extensive organic-rich shales were deposited across much of North America (Woodrow et al., 1973).

Stratigraphically, as shown in Figure 2.2, the Chattanooga Formation lies unconformably over the Hunton Limestone and is directly beneath the Sedalia Dolomite (Barrick et al., 1990).

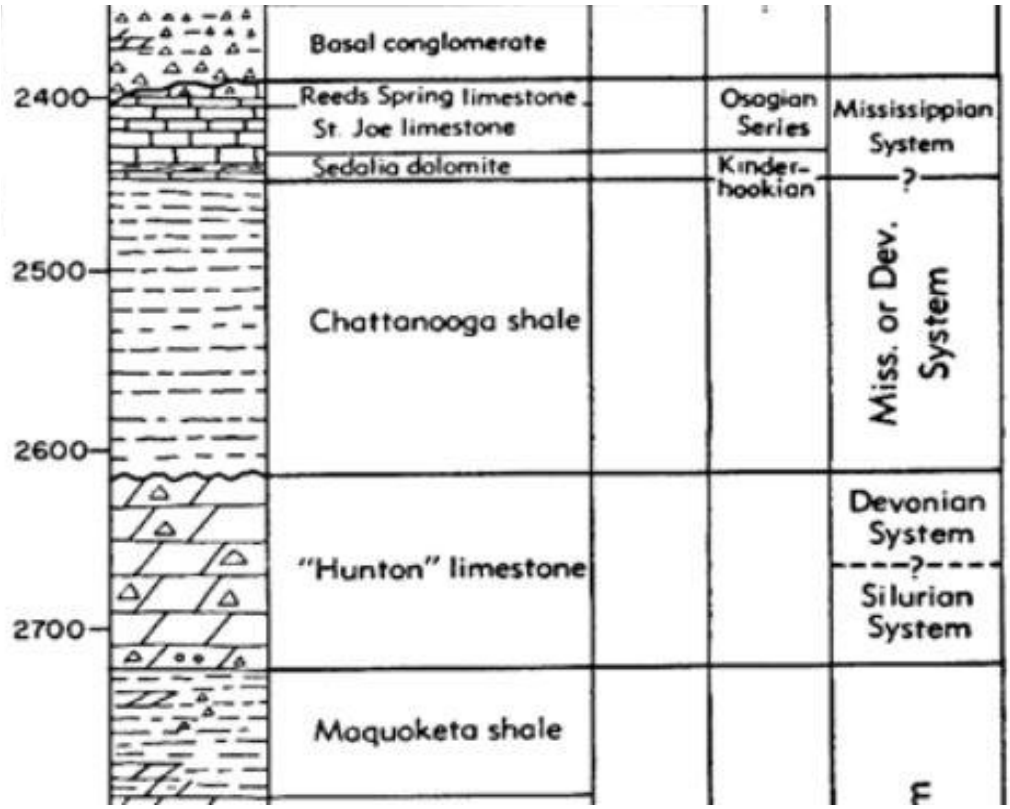

Figure 2.2: Stratigraphic column of the Chattanooga Formation (here called "Chattanooga Shale") and the surrounding units (Shenkel, 1955).

In terms of the petroleum system, the Chattanooga Formation acts both as a source rock and a reservoir rock (Cardott et al., 2015). As a source rock, it is comprises type II kerogen; the ideal type for producing oil as well as gas (Cardott et al., 2015). Type II kerogen forms from pollen/spores from land plants, marine plankton, and some land plant components (Cardott et al., 2015). The average total organic content is 5.4 ± 6.9 wt% (Comer and Hinch, 1987), with a vitrinite reflectance (Ro) of between 0.5 and 0.7 Ro (Higley, 2014).

The Chattanooga Formation also makes a suitable unconventional reservoir rock, because it is rich in biogenically-produced silica (Cardott et al., 2015), which makes it relatively brittle. This characteristic makes this shale susceptible to both natural and induced fractures that result in increased porosity and permeability (Cardott et al., 2015). Nano-porosity is created in the post-oil solid bitumen, which is ideal for gas storage and migration (Cardott et al., 2015).

Chapter 3 - Methods of Investigation

The methods used to investigate the Douglas County core included facies descriptions aided by qualitative petrography, the collection of hand-held x-ray fluorescence (HHXRF), inductively-coupled mass spectrometry (ICP-MS), LECO carbon/sulfur (LECO C/S), and x-ray diffraction (XRD) point data, and a cross correlation analysis of important indices using the wavelet transform method in MATLAB.

Facies Analysis Aided by Qualitative Petrography

A detailed facies analysis of core 15-045-21557 from Douglas County, Kansas was performed at the mm-cm scale based on procedures from Lazar et al. (2015). Facies descriptions included textural and compositional characteristics, sedimentary structures, degree of bioturbation and other features that reflect variability and possible cyclicity in the shale deposit. The core was initially inspected to ensure that the stratigraphic order and orientation of the core samples were correct. It was then split in half vertically using a rock saw in order to expose a flat surface on the core to make the identification of the sedimentary features easier. The core was cleaned to remove any excess drilling mud or debris adhering to the core as a result of drilling or cutting of the core with a wet, soft sponge and then dried immediately with a paper towel. The cleaned core was then photographed in its entirety.

The examination of the core started with looking at the whole core at a larger scale, making notes of changes in thickness, texture, composition, continuity and identifying key stratigraphic surfaces (e.g. maximum flooding surfaces). Core descriptions were carried out at a millimetric to centimetric scale to assure high resolution results, observing the texture, bedding, and composition. Texturally, mudstones in the core were subdivided into coarse, medium, or fine mudstone, based on the scratch test (Lazar et al., 2015). Visually, mudstones are recognized by having less than 50

percent sand-sized grains. Scratch tests are effective for identifying the composition of a sample. The different coloring and luster of the powder generated by a scratch test can be used to identify whether the mud is fine, medium or coarse (Lazar et al., 2015). Bedding descriptions include laminae, physical sedimentary structures, biological sedimentary structures such as burrows and fossils. The degree of carbonate present was tested by performing a scratch test and dropping dilute hydrochloric acid on the powder. The vigor of the reaction of the scratched surface versus the unscratched core will be used to estimate the amount of calcite in the sample. The data were recorded consistently using "Forms for Capturing Mudstone Descriptions in Cores" from Lazar et al. (2015), shown in Figure 3.1.

Facies were identified based on grainsize, color, texture, degree of bioturbation, fissility, mineralogy, and types of organic matter present. Bioturbation was recorded on a scale from 1 to 4, with increasing numbers representing a higher degree of bioturbation. In terms of fissility, if present, three categories were used, based on the spacing between fissility planes. Fine fissility refers to less than 1 cm, medium refers to between 1 and 3 cm and coarse is greater than 3 cm. The fine-grained nature of the Chattanooga Formation made initial observation of the mineralogy difficult, later refined with petrography and XRD. Like the mineralogy, the type of organic matter was more easily differentiated between the facies through petrography.

All data collected were then summarized into a sedimentary log and facies table. The sedimentary log includes the depths of occurrence for each facies, grain size, sample locations, degree of oxygenation and type of organic matter (palynofacies). The log was constructed at a scale at which 1.25 inches is equal to 1 foot, and was then redrawn in Adobe Illustrator. The facies table includes a description of each facies, its color in the core, and the types of organic material present, as well as interpretations of the depositional conditions and the degree of oxygenation.

Following the facies analysis, key stratigraphic surfaces, such as sequence boundaries, were identified by abrupt facies changes, aided by the chemostratigraphic data.

Based on macroscopic core descriptions, a total of 19 samples, representative of the facies variations along the core, were collected for petrographic and/or complementary analysis (Table 3.1). The thin sections were examined using a conventional polarizing optical microscope with an attached high-resolution camera. Regular photomicrographs were taken in the conventional petrographic microscope, and photomicrographs of the entire thin section were taken using a Raman microscope in conjunction with the Wire 2.0 software's montage feature.

Sample depth (ft)	Petrographic analysis	XRD	ICP-MS	LECO C/S
1638.5	X		X	X
1641.5	X	X		
1642.3	X			
1643			X	X
1643.6	X			
1645			X	X
1648			X	X
1651			X	X
1655			X	X
1656.3	X	X		
1666			X	X
1667			X	X
1668.5	X	X		
1668.7	X	X		
1668.9	X	X		
1674			X	X
1675.2	X	X		
1676.5			X	X
1677.3	X	X		

Table 3.1: Samples collected in the Douglas County core for petrographic and/or complementary analysis.

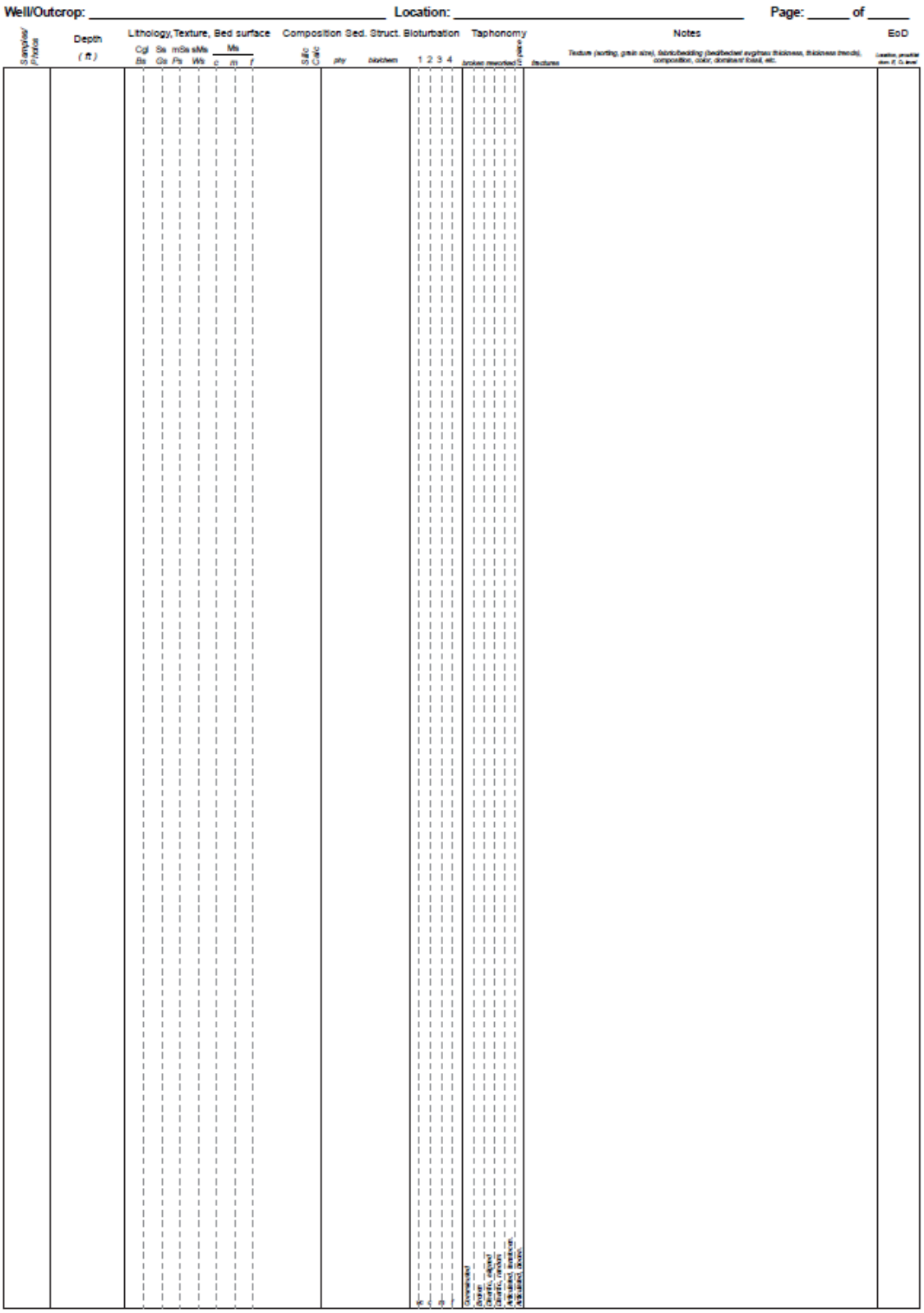

Figure 3.1: Form used for detailed core description of mudstones (Lazar et al. 2015).

XRD Analysis

Bulk and clay fraction XRD analyses were performed on seven samples. Sample preparation for bulk and clay fraction XRD analyses required different procedures, described below and detailed in Appendix B. All samples were analyzed using a Malvern Panalytical Empyrean XRD machine.

Samples for bulk analysis must be finely powdered. To get the solid rock samples from the core to a powder, they were initially crushed using a small sledge hammer. To avoid contamination, the samples were placed between two new, clean sheets of paper and hit just hard enough with the hammer to break the sample into pebble-sized pieces. The pebble-sized pieces were then powdered finely using a mortar and pestle. To ensure no cross-sample contamination, the mortar and pestle were both rinsed with deionized water and then wiped down using alcohol between samples.

The resulting powder was taken to the diffractometer and scanned between two theta values of 5 and 70 degrees. The XRD data were processed using the High Score Plus software package and the recommended steps in the procedure designed by Speakman (2012).

Sample preparation for clay fraction XRD analysis followed a modified procedure from Kübler at the University of Neuchâtel (Kübler and Jaboyedoff, 2000). For comprehensive clay fraction analysis, two separate clay fractions must be collected, between 2-16 μm and less than 2 μm. For this, unlike the bulk XRD analysis, the samples need to be only crushed, not powdered. Again, crushing was done by placing the sample in between two pieces of clean paper and lightly hitting them with a small sledge hammer until the samples were in small pebble-sized pieces. Carbonate material was removed from the samples using 10% hydrochloric acid. Samples were then washed with deionized water, then centrifuged at 5000 rpm's in 10-minute sessions until the

remaining acid was removed. The washed samples were then separated into two clay fractions (less than 2 microns and between 2-16 microns) based on centrifuge time. One slide for each clay fraction was prepared for each sample. After the initial XRD analysis, the slides were exposed to ethylene glycol at 60 degrees Celsius for a duration of 24 hours in order for the samples to absorb the vapor and test for expanding clays (ex. smectite). The clay fraction data were analyzed using the MacDiff 4.2.5 software because of its extensive clay mineral database with interpretations aided by Moore and Reynolds (1997).

HHXRF, ICP-MS, and LECO C/S

Hand-held X-ray fluorescence (HHXRF) analysis was used to generate a high-resolution chemostratigraphic dataset that includes the concentrations of elements typically used as proxies for sediment source, productivity, and degree of oxygenation at the time of deposition (Tribovillard et al., 2006; Sageman and Lyons, 2004). Measurements along the core were taken every 4 inches (~10 centimeters), with a standard tested between every eleventh and twelfth sample to ensure that accurate measurements were still being recorded. The HHXRF that was used to detect concentrations of major, minor and trace elements is a Bruker Trace III. Major elements included Al, Ca, K, Si, Ti, and minor/trace elements included Ba, Cu, Mo, Ni, and Zr. To test for the major elements, the HHXRF must be set up without a filter, with the vacuum pump active, and running at 15kV and 25μA for 180 seconds. The vacuum pump is used for major elements to increase the intensity of the analysis for elements with lighter masses. Trace elements were analyzed with a yellow filter in the machine, without the vacuum active, and running at 40kV and 12.4μA for 120 seconds. The concentrations were calculated using the Bruker mudrock calibration and the standard used was RTC-WS-220 (Rowe, 2012).

These data were used to generate chemostratigraphic logs that allowed the study of elemental variation with depth in the core. All of the elemental concentrations were normalized to aluminum to subtract the contribution from continental input and variations on sedimentation rates. For this study, Ti/Al, Zr/Al and Si/Al were used as proxies for detrital input (Sageman and Lyons, 2004; Bhatia and Crook, 1986; Pearce and Jarvis, 1992; Pearce et al., 1999; Sageman and Lyons, 2004); Ba/Al and P/Al were used as proxies for primary productivity (Tribovillard et al., 2006); Cu/Al, Fe/Al, Mo/Al, Ni/Al and Zn/Al were used as proxies for anoxia (Morford et al., 2005).

Ten samples were taken for complementary analyses, including Inductively-Coupled Plasma Mass Spectrometry (ICP-MS) and LECO carbon/sulfur analysis. Total organic carbon (TOC) and sulfur concentrations were measured in a LECO C/S analyzer by GeoMark Research. ICP-MS sample preparation and analysis were carried out in the GeoAnalytical Lab at Washington State University. This analysis aimed at testing the accuracy of the HHXRF data, as well as providing the U concentration (not accurately measured by the HHXRF). Accuracy was tested by plotting the concentrations collected by both the ICP-MS and HHXRF at same depths against each other to determine the linear correlation.

The HHXRF and ICP-MS data were used to calculate enrichment factors for Co, Cu, Mo, Ni, U, and Zn in the Chattanooga Formation in comparison with elemental concentrations of the average shale. According to Tribovillard et al. (2006) and Huang et al. (2011),

Enrichment Factor = Measured Elemental Concentration/ Average Shale Elemental Concentrations

Average shale concentrations used to calculate the enrichment factors are from Wedepohl et al. (1991). Enrichment factors along the Chattanooga Formation in the study core are shown as logs,

except for U, recorded as point data, since its concentration was measured only in ICP-MS analysis.

Cross-Correlation Through Wavelet Transform

Wavelet transform is a multi-resolution technique that allows analysis of data at multiple scales and resolutions. Accordingly, a cross-correlation analysis was done using the wavelet transform method between index responses derived from the HHXRF data. The main purpose was to investigate whether there might be correlation among various elemental indices, used as proxies, at different depths and scales (periods). To perform the wavelet transform procedure, a code from Grinsted et al. (2004) was executed using MATLAB. The detrital indices examined were Si/Al, Ti/Al, and Zr/Al. The productivity indices examined were Cu/Al, P/Al, and Zn/Al.

The cross correlation was executed between indices used as proxies for the same depositional conditions. The output from the MATLAB code is a figure that provides data on how correlated two datasets that use the same data for their X-values and different values for their Y-values. For our purpose, the depths in the core where the HHXRF data points were measured are the X-values and the index responses at those depths are the Y-values. The X-axis displays the depth in the core being considered, and the Y-axis is the period (scale) at which the correlation occurs. The degree of correlation is given by the color bar. Warmer colors refer to strong correlations, whereas cold colors refer to weak correlations. In each figure, only the areas that are not faded out can be considered. The faded areas include correlations that cannot be detected due to the scale at which the correlation is being made and the total length of the core. The black arrows in the background of these figures are not being used for the purpose of this study. The goal for this method is to detect correlations between indices that are too difficult to see with the human eye.

Chapter 4 - Results and Interpretation

Facies Analysis

Detailed facies description and petrographic analysis allowed the identification of nine facies (Table 4.1). Facies codes represent the different lithologies (Ss = sandstone, Ms = mudstone) and grain sizes (c = coarse, m = medium, f = fine). The distribution of these facies in the study core is displayed in Figure 4.1. Figures 4.2 through 4.8 show each facies at multiple scales, including a core photo, a photomicrograph of the complete thin section captured using the Raman microscope, and photomicrographs under cross- and plane-polarized light from the thin sections.

The close examination of the nine facies showed that most of them are depositional facies, but two are diagenetic facies (cMs and mMs). The depositional facies (cSs, fMs-1, fMs-2, fMs-3, fMs-4, fMs-5, and fMs-6) are ordered from proximal to distal in Table 4.1, based on grain size and type of organic matter (terrestrial vs. amorphous/algal).

The most proximal facies is cSs. It consists of intraclastic, coarse sandstones with quartz grains and mud clasts (Figure 4.2); the latter were compacted to form a pseudomatrix. In some portions the mud pseudomatrix is replaced by pyrite. The coarse grain size in this facies and the presence of mud rip-up clasts indicates a high-energy environment, either by currents or waves. Organic material was not found in this facies, likely due to the high energy in the system leading to increased oxygen levels. This favors the oxidation of organics and render the environment more inhabitable for organisms that consume the organic material.

The six fMs facies display all variations of the fine mudstones that make up most of the Chattanooga Formation. Despite having similar grain sizes, other attributes indicate that these

Depositional Facies					
Facies Code	**Facies description**	**Color**	**Organic Material**	**Interpretation**	**Oxygenation**
cSs	Intraclastic coarse sandstone, bioturbated BI 1; large mud intraclasts with Tasmanites; phosphate bioclasts; large pyrite nodules	Olive gray		Reworking in high-energy environments by currents or waves	ox
fMs-1	Fine mudstone, with symmetric ripples, truncations and scour surfaces; (pyrite nodules)	Brownish black		Gravitational settling of mud with weak reworking by waves	ox-sub
fMs-2	Fine mudstone, massive, medium-coarse fissility, organic-poor, with phytoclasts, BI 1-3 (increasing to top); replaced by Fe microdolomite, Pyrite nodules	Grayish black	Phytoclasts	Gravitational settling of mud and organics, with high continental input (plant debris)	sub
fMs-3	Fine mudstone, 'crumbly', fine fissility, centimetric alternation of silty, organic-poor, bioturbated laminae BI 1-3 and organic-rich ones (AOM and some phytoclasts); replaced by Fe microdolomite	Black	AOM, Phytoclasts	Gravitational settling of mud and organics, under longer-lived, alternating energy and oxygen levels, high productivity	sub
fMs-4	Fine mudstone, laminated, medium fissility, with mm silt laminae and scattered silt grains, organic-rich (abundant Tasmanites and AOM, rare phytoclasts), BI 1-2	Brownish black-olive gray	AOM, Tasmanites, (Phytoclasts)	Gravitational settling of mud and organics under very high productivity conditions, with short-lived clastic input and increased oxygen levels	sub-an
fMs-5	Fine mudstone, organic-rich to org-poor, with Tasmanites and optical fissility (fine-medium); laminated to massive, mm variable bioturbation (BI 1, increasing to top), pyrite nodules; at 1656.5 ft, displaced by mm calcite veins	Dark gray	AOM, Tasmanites, (Phytoclasts)	Gravitational settling of mud and organics, under high productivity, dysoxic conditions, with frequent episodes of aeration and bioturbation; local displacement by diagenetic calcite	sub-an
fMs-6	Fine mudstone, 'flaky', fine fissility, with scour surfaces; BI 1	Olive gray	AOM, Tasmanites	Gravitational settling of mud and organics, under high productivity, anoxic conditions	anoxic
Diagenetic Facies					
cMs	Microdolostone with mm bands of dark mudstone; completely cemented, scattered bioclasts; fluidization structures	Olive gray		Gravitational settling of mud, followed by almost complete replacement by microdolomite	
mMs	Medium mudstone extensively cemented/replaced by Fe microdolomite, with medium fissility, sparse large pyrite nodules; BI 2-3	Dark greenish gray		Gravitational settling of mud, followed by extensive replacement by microdolomite	

Table 4.1: Facies table with the description and interpretation of the nine facies identified in the studied core. Abbreviations used in this table include ox = oxic, sub = suboxic, an = anoxic, BI = bioturbation index, and AOM = amorphous organic matter

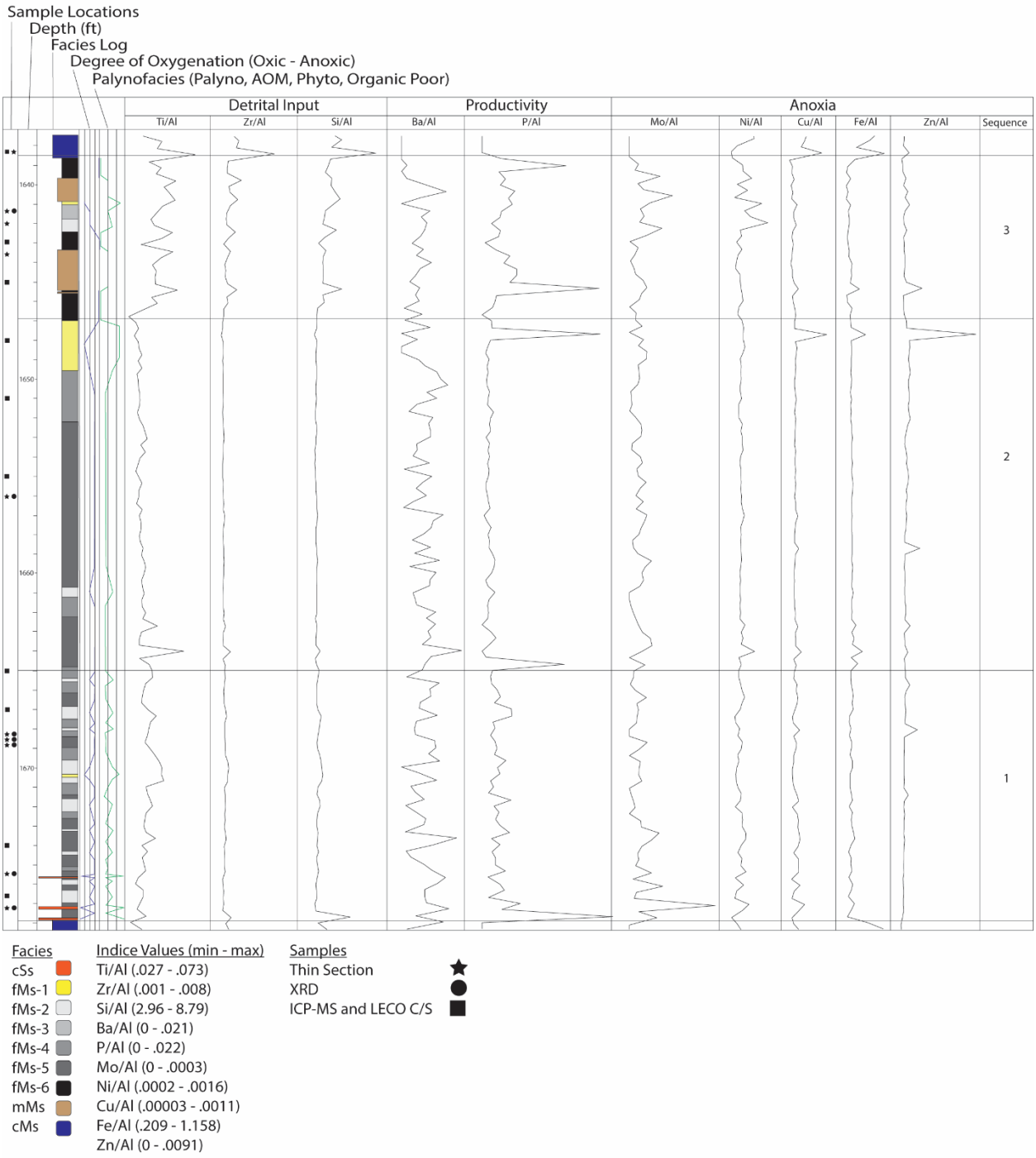

Figure 4.1: Digitized sedimentary log of the Chattanooga Formation in the Douglas County core (API: 15-045-21557) with marked sample types/locations, oxygenation and organic matter profiles, chemostratigraphic indice profiles and designated sequence boundaries.

mudstones were deposited under slightly variable depositional conditions, albeit with consistently low-energy.

Facies fMs-1 lacks organic matter and displays subtle sedimentary structures such as small, slightly asymmetrical ripples (Figure 4.3). The ripples suggest weak reworking by distal currents, responsible for an increase in oxygen levels that favor the oxidation of organic matter. This interpretation puts this as the most proximal of the fMs facies.

Facies fMs-2 comprises organic-poor, fine mudstones, with medium to coarse fissility and Fe-rich dolomite replacement (Figure 4.4). The organic material in this facies is mostly phytoclasts, plant debris used as a proxy for continental input. The high abundance of phytoclasts indicate substantial contribution from terrestrial sources, and thus suggest relatively more proximal settings.

Facies fMs-3 consists of a centimeter-thick alternation of silty, organic-poor, bioturbated laminae and organic-rich laminae with scattered silt grains (Figure 4.5). The alternation of the organic-rich and organic-poor zones, accompanied by respectively lesser and higher silt content, can be explained by recurrent episodes of high-productivity, low-energy and low-oxygen levels, alternated with higher-energy, longer-lived aeration intervals. High productivity, along with low oxygen levels, would account for the preservation of the organic material that includes both amorphous organic material (AOM) and some phytoclasts. An increase in energy levels due to current or wave action would transport coarser sediments (silt) and drive the oxygen concentration up. A transition from anoxic to oxic would favor increased activity of organisms in the environment, which in turn explains the increased bioturbation in organic-poor, silty layers.

The overall mud to silt ratio tends to increase distally. Facies fMs-4 comprises fine, laminated mudstones with medium fissility, scattered silt grains and millimetric silt laminae

(Figure 4.6). The organic matter consists of *Tasmanites*, along with AOM and rare phytoclasts. The diversity and abundance of organic materials suggest a low-energy, high productivity setting with rare, short-lived continental input, responsible for the deposition of silt laminae and increased oxygen levels.

Facies fMs-5 is composed of fine mudstones with variable organic content (poor to rich) and optical fissility in thin section (Figure 4.7). Like fMs-4, most of the organic matter consists of AOM, *Tasmanites*, and occasional phytoclasts. The degree of bioturbation is lower than fMs-4 and small pyrite nodules are common. The optical fissility, low bioturbation index and abundance of labile organic matter is interpreted as resulting from deposition in low-energy, high-productivity and anoxic settings.

Facies fMs-6 is composed of fine mudstones with fine fissility, and a 'flaky' texture macroscopically (Figure 4.3). The organic matter in this facies comprises of AOM and *Tasmanites* only, with no evidence of phytoclasts, which suggest more distal settings. The abundance and type of organics preserved suggest that this facies formed in low-energy, distal environments under high productivity that favored anoxic conditions.

The two diagenetic facies include cMs and mMs. Both of these facies are fine mudstones that were replaced by Fe-rich dolomite during diagenesis (Figure 4.8). Crystal size of the replacive dolomite led to apparent increase in grain size compared with the original mud that was replaced, and also served as a criterion to distinguish between cMs and mMs. The cMs facies is extensively cemented and replaced, but scattered bioclasts and millimetric bands of dark mudstones are still visible. The mMs facies is slightly less cemented and replaced than cMs, with medium fissility and sparse pyrite nodules. Due to the nearly complete replacement of the mudstones by Fe-rich dolomite, there is no evidence of the type of organic material in these sediments.

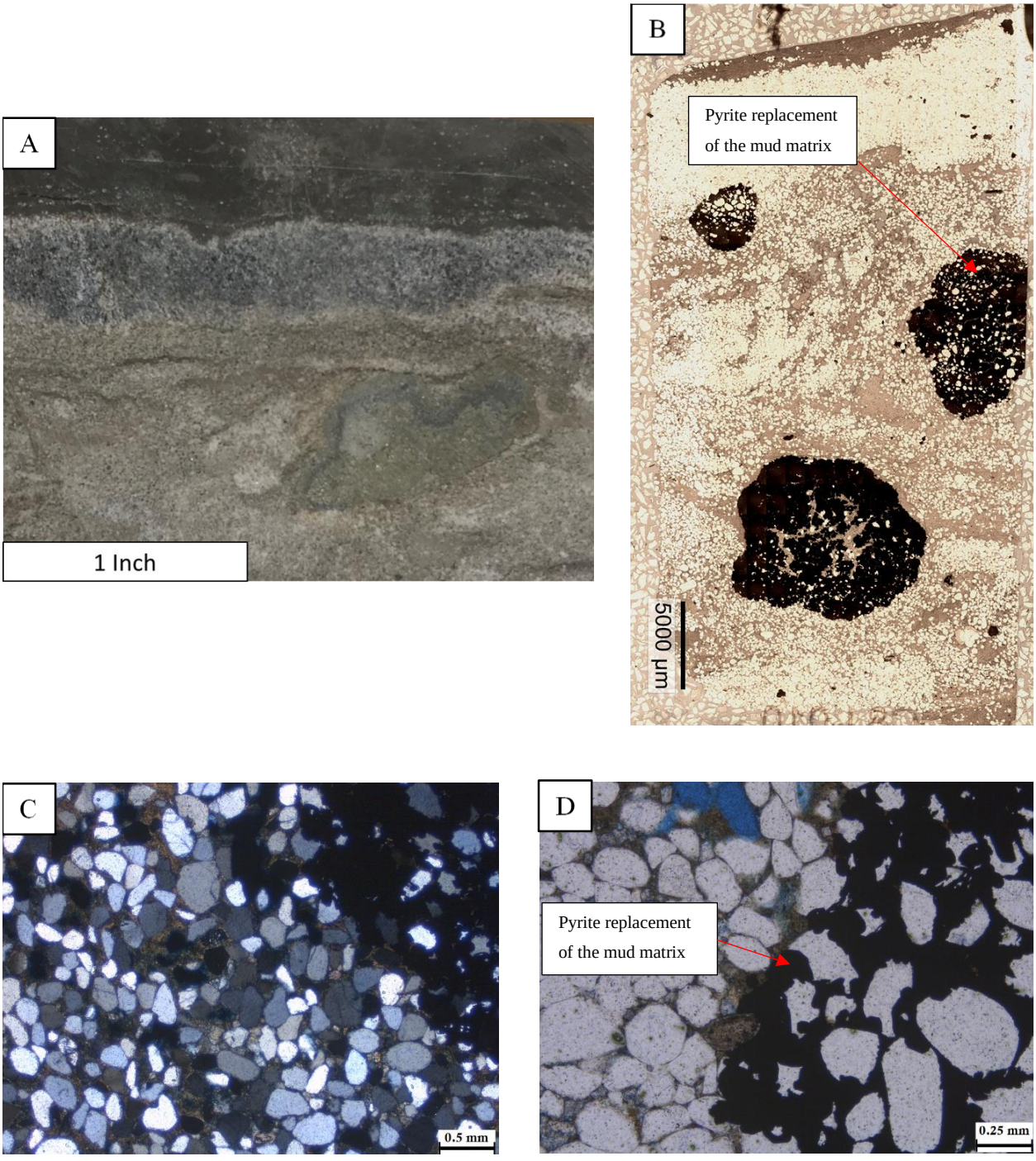

Figure 4.2: Representative photos of facies cSs; Core photo (A); Raman photomicrograph (B); Optical photmicrograph, (obj 2.5x) under XPL (C) and (obj 5x) under PPL (D). Coarse grained sandstone consisting of quartz in a mud pseudomatrix. The mud is replaced in some areas by pyrite (opaque sections).

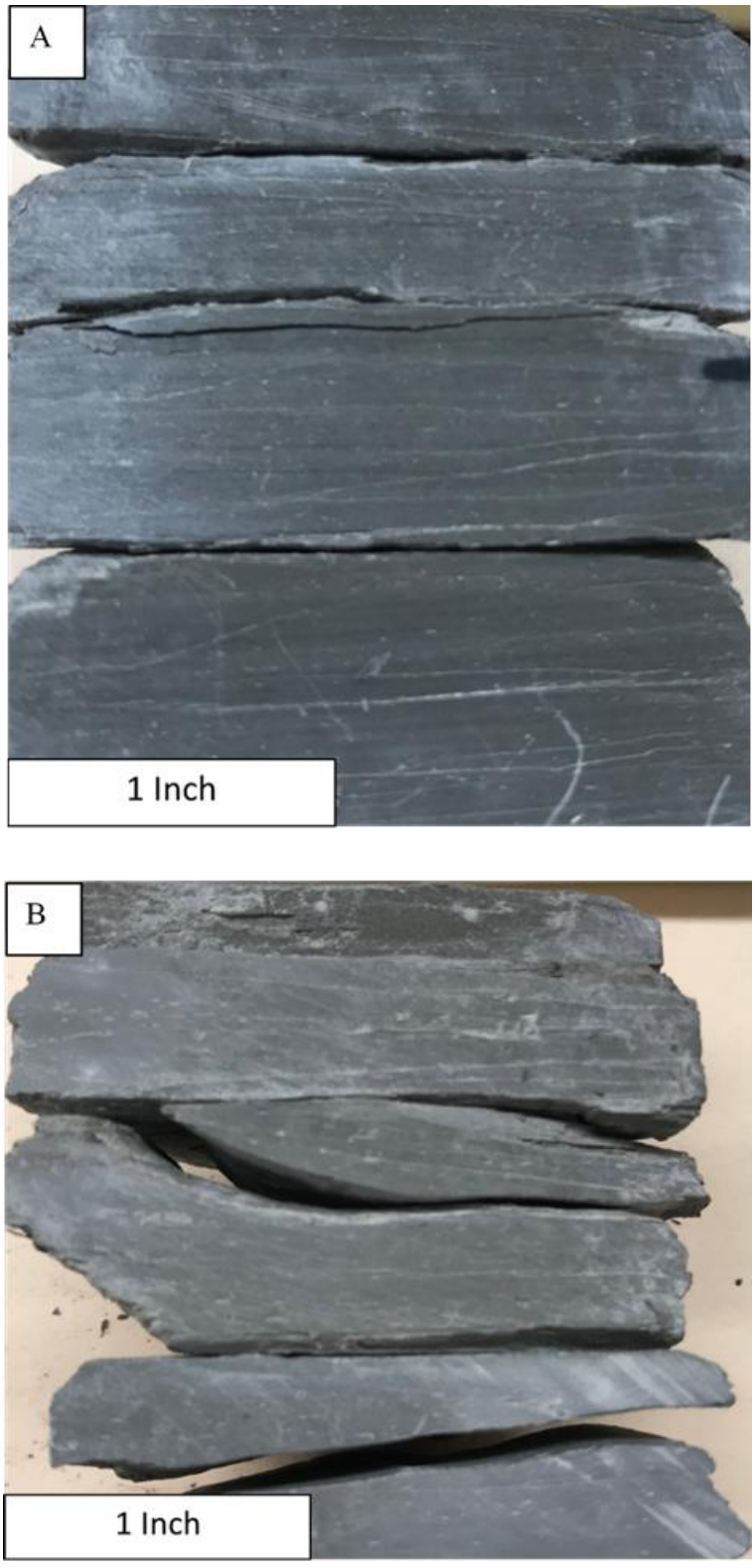

Figure 4.3: Representative core photos of facies fMs-1 (A) and fMs-6 (B). fMs-1 displays few sedimentary structures suggesting a slight reworking of sediments. fMs-6 has fine fissility and a flakey texture, with AOM and *Tasmanites.*

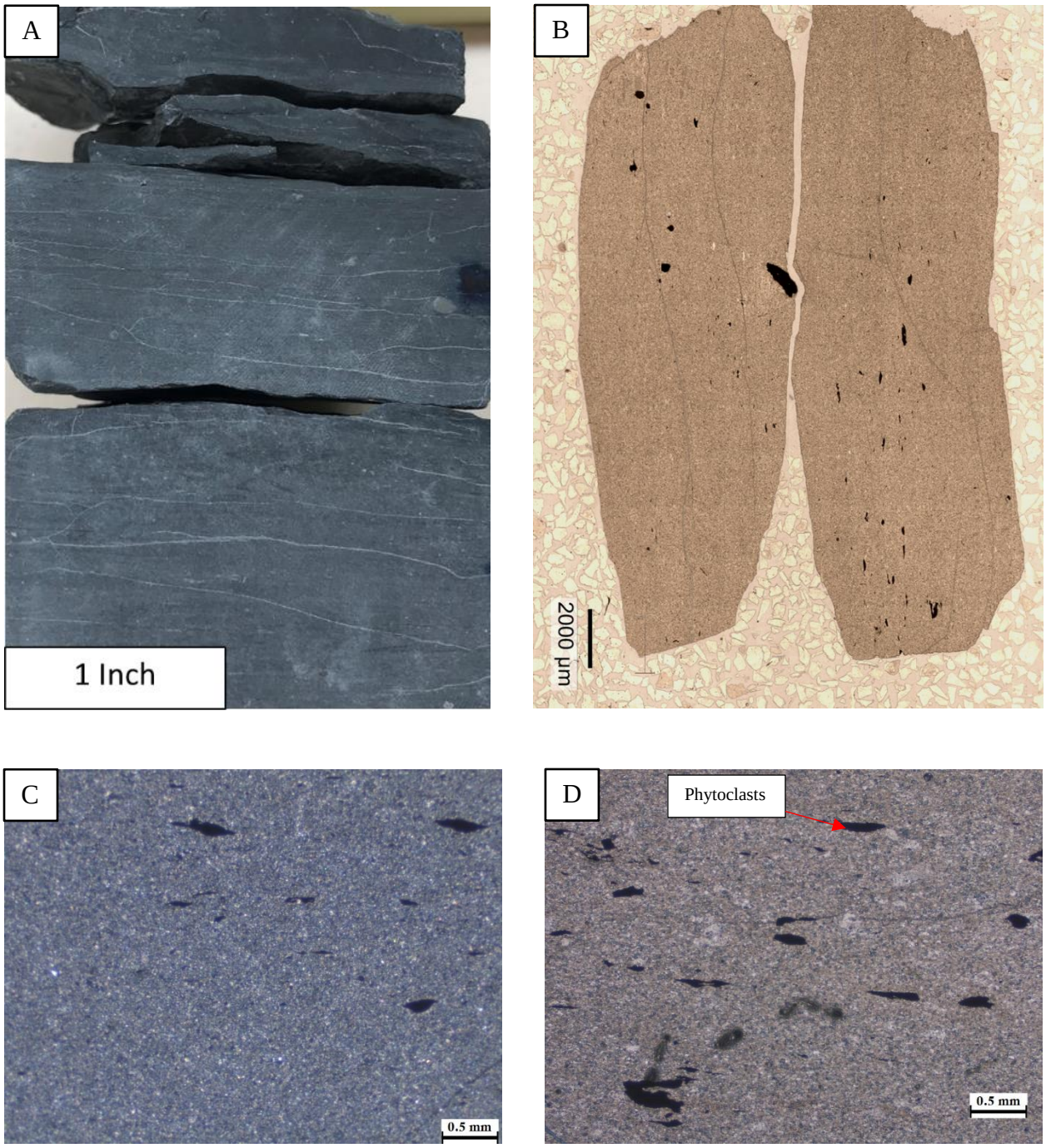

Figure 4.4: Representative photos of facies fMs-2; Core photo (A); Raman photomicrograph (B); Optical photomicrographs (obj. 2.5x) under cross polarizers (XPL) (C) and plane polarizers (PPL) (D). Opaque portions of the photomicrographs are phytoclasts (plant debris) and the mud is matrix is replaced by Fe-rich dolomite (blue).

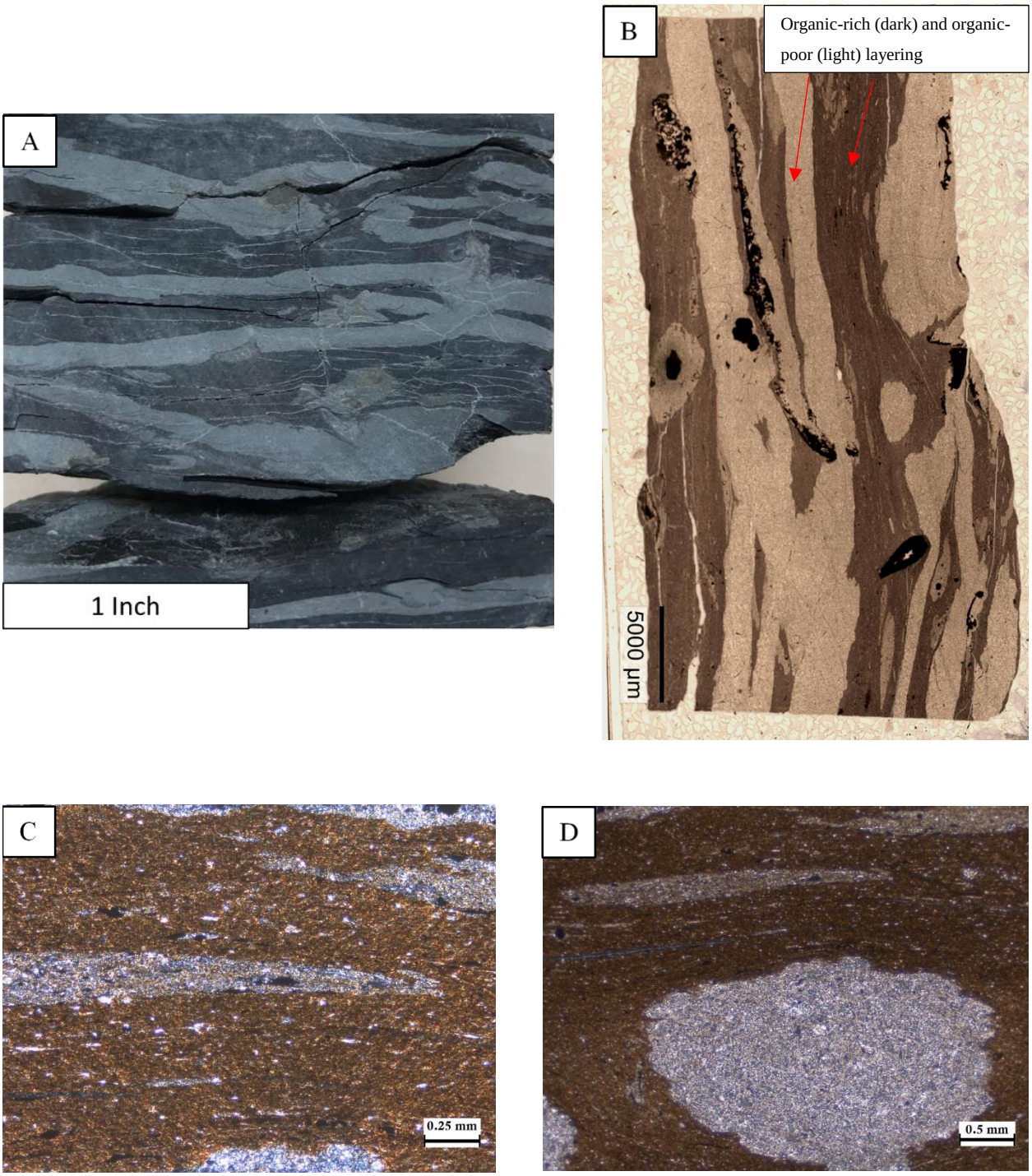

Figure 4.5: Representative photos of facies fMs-3; Core photo (A); Raman photomicrograph (B); Optical photmicrograph,(obj 5x) under XPL (C) and (obj 2.5x) under PPL (D). Centimeter-thick alternations of silty, organic-poor, bioturbated laminae (light colored) and organic-rich laminae (dark colored).

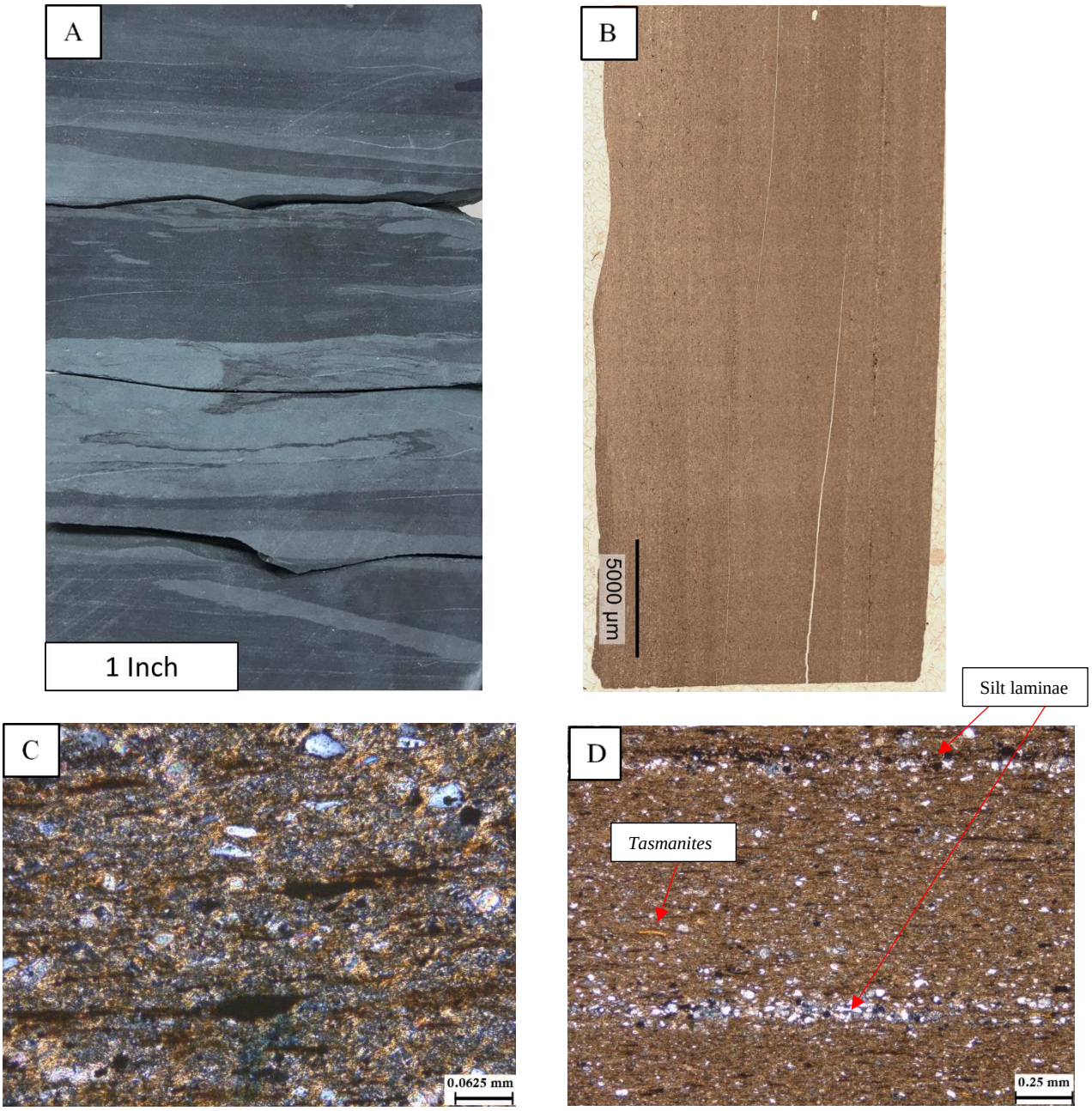

Figure 4.6: Representative photos of facies fMs-4; Core photo (A); Raman photomicrograph (B); Optical photmicrograph,(obj 20x) under XPL (C) and (obj 5x) under PPL (D). Fine, laminated mudstones with medium fissility, scattered silt grains and millimetric silt laminae. The organic matter consists of *Tasmanites*, along with AOM and rare phytoclasts.

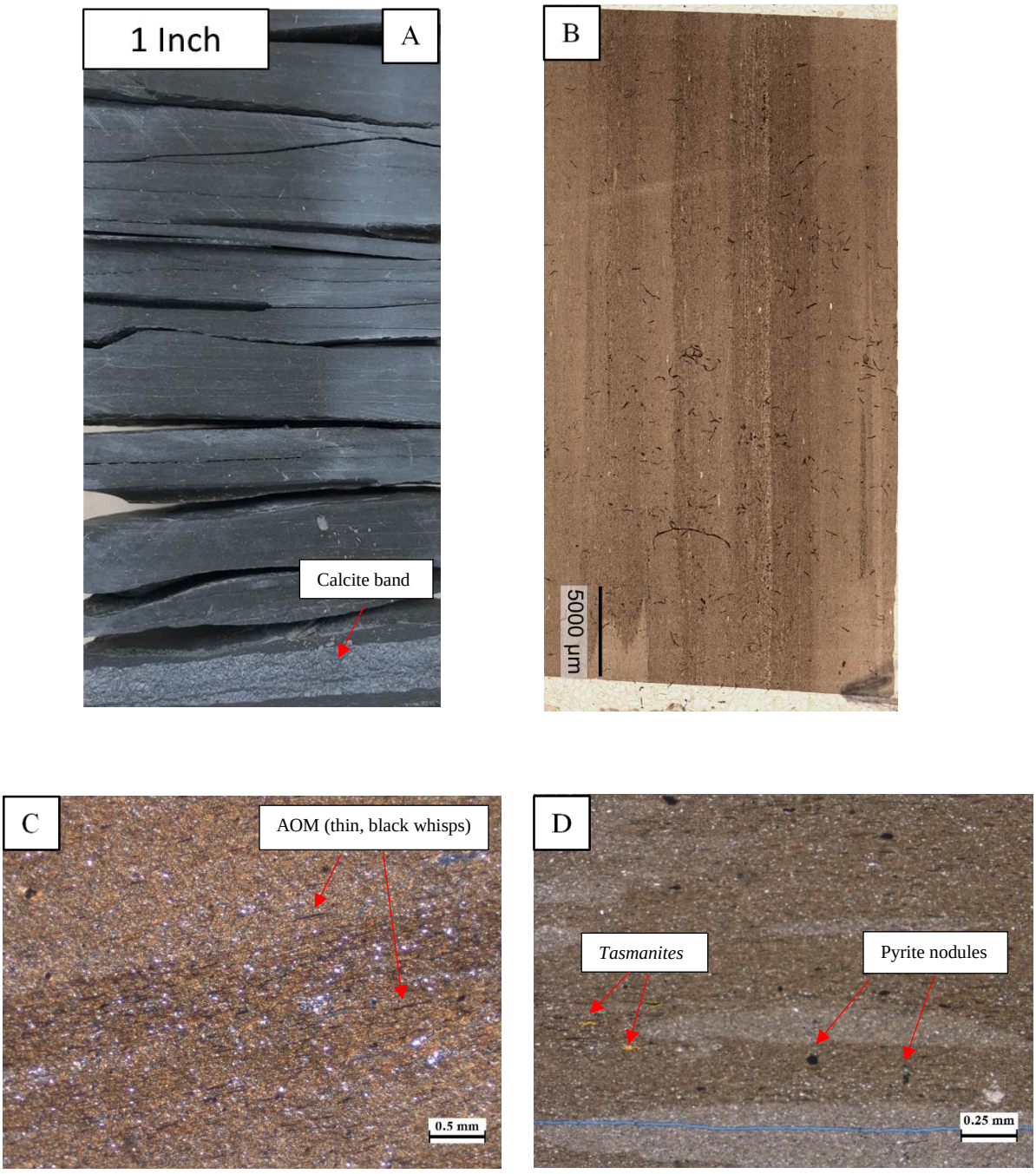

Figure 4.7: Representative photos of facies fMs-5; Core photo (A); Raman photomicrograph (B); Optical photmicrograph,(obj 2.5x) under XPL (C) and (obj 5x) under PPL (D). Fine mudstones with variable organic content (poor to rich). Organic matter consists of AOM, *Tasmanites*, and occasional phytoclasts.

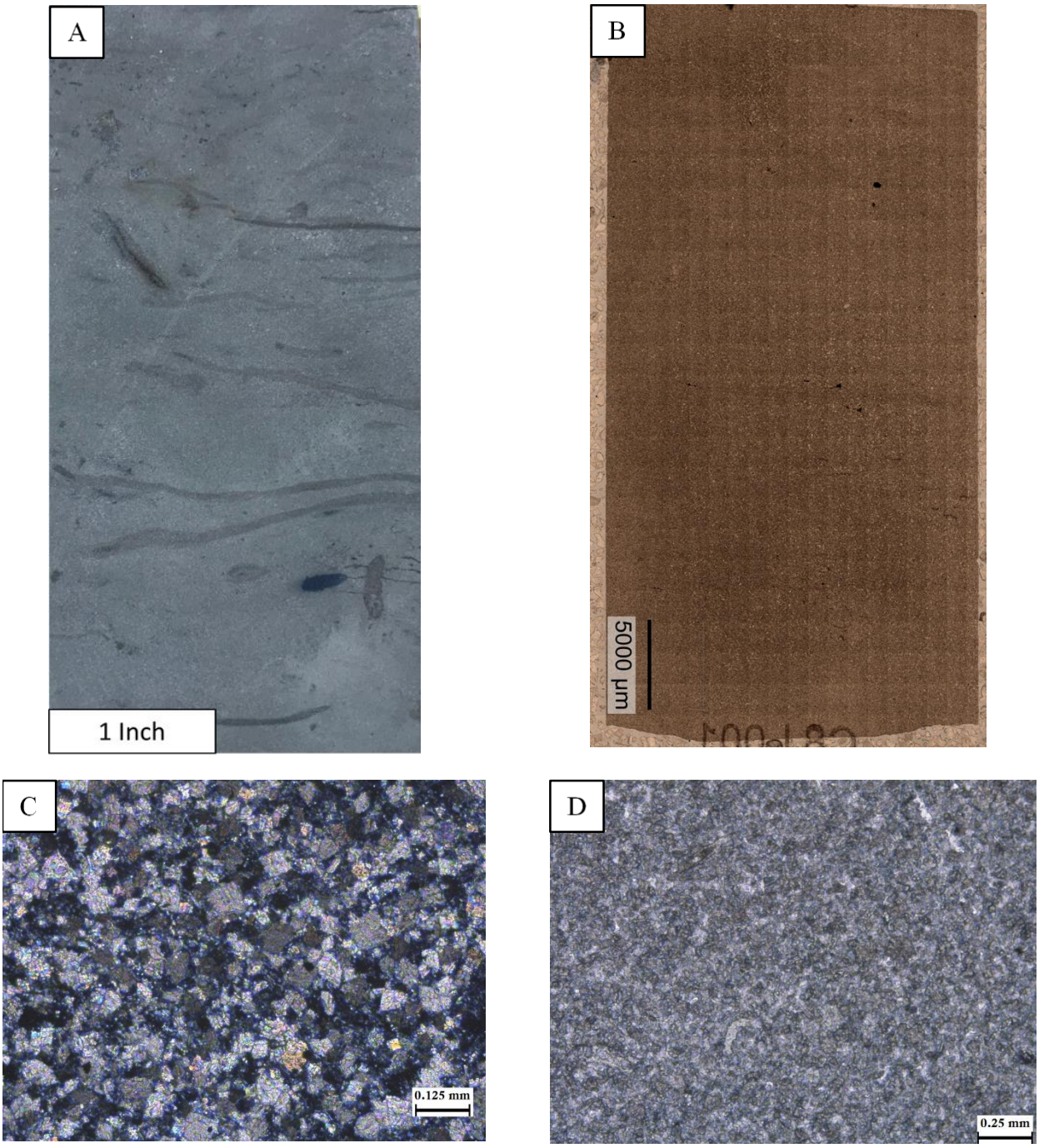

Figure 4.8: Representative photos of facies mMs; Core photo (A); Raman photomicrograph (B); Optical photmicrograph,(obj 10x) under XPL (C) and (obj 5x) under PPL (D). Fine mudstone that was replaced by Fe-rich dolomite during diagenesis, increasing the grain size.

XRD Analysis

The diffractograms for all seven XRD samples are displayed in Figure 4.9. Six of the seven samples displayed nearly identical results, and thus can be represented by Sample DCC - 1641.5. Only Sample DCC – 1656.3 (pink) displayed a slightly different XRD spectrum, requiring separate data processing. Figures 4.10 and 4.11 show the individual spectra and minerals identified in samples 1641.5 and 1656.3, respectively. The primary minerals found in the bulk analysis for all of the samples are quartz and muscovite. The six samples represented by DCC - 1641.5 also include pyrite, while Sample DCC – 1656.3 shows the presence of calcite.

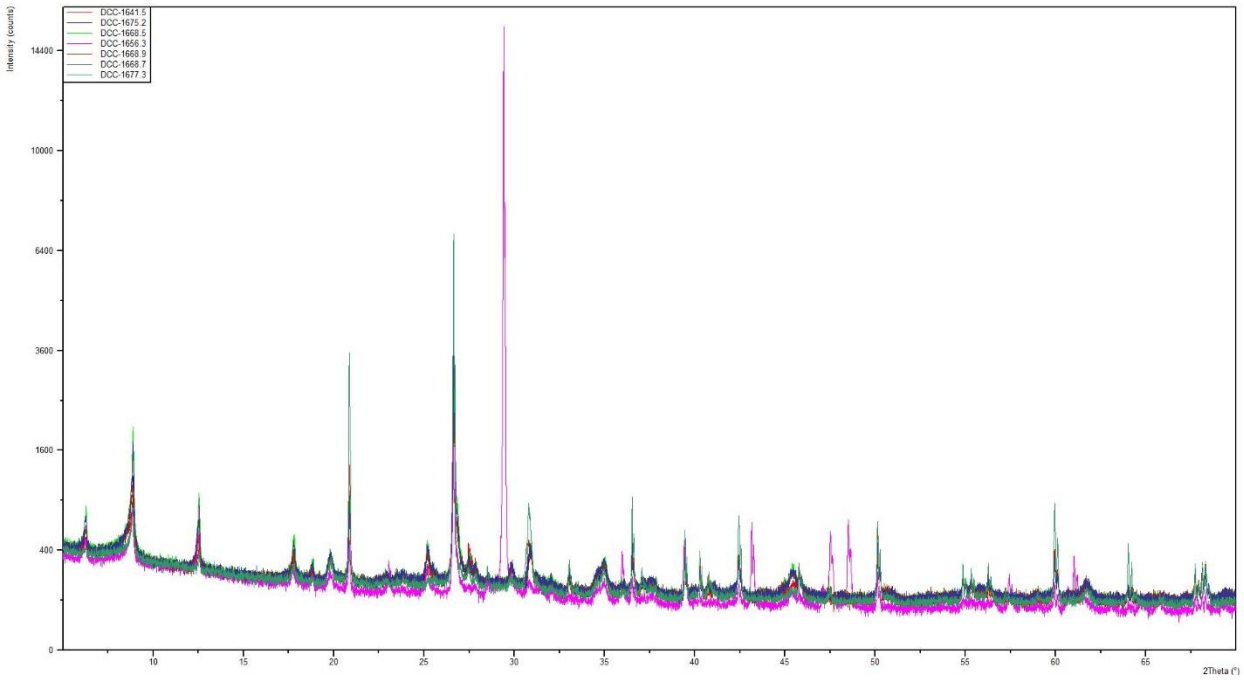

Figure 4.9: Diffractograms for all seven samples ran for bulk XRD analysis.

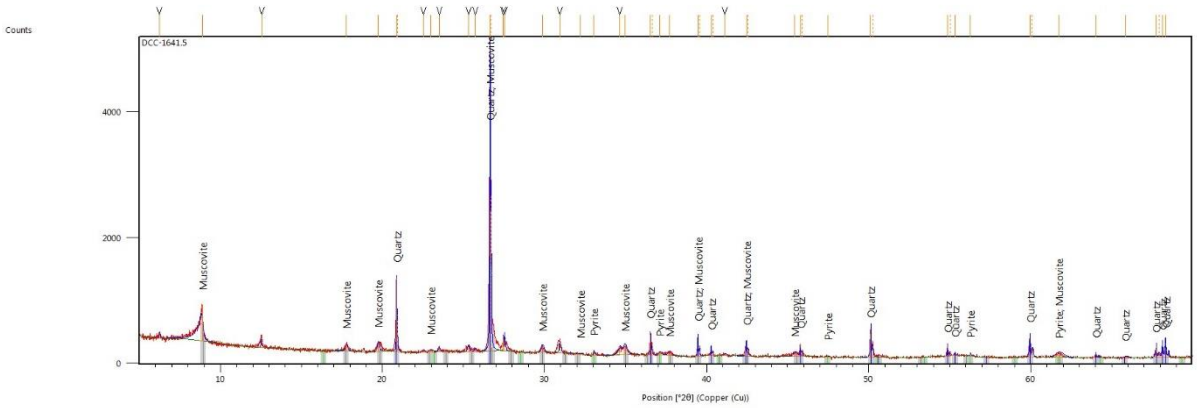

Figure 4.10: Diffractogram for Sample DCC – 1641.5, with the identification of peaks that indicate the mineralogy.

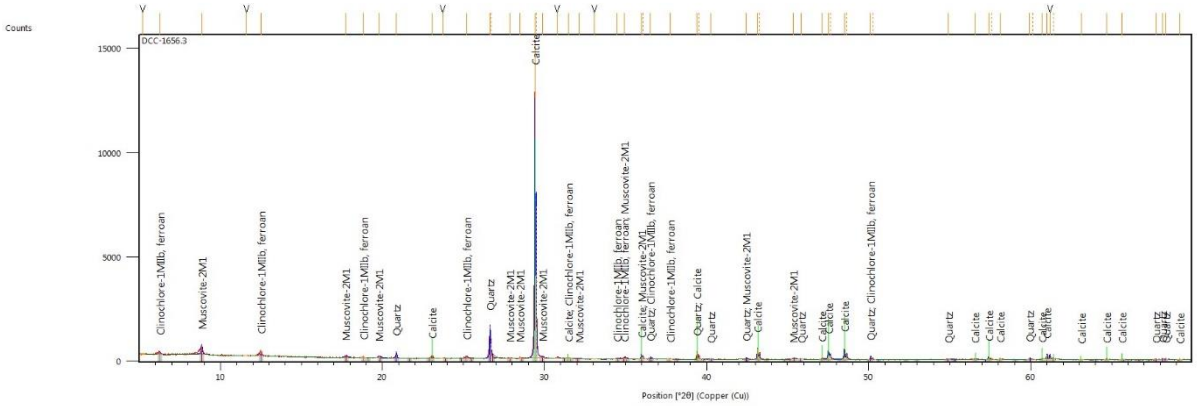

Figure 4.11: Diffractogram for Sample DCC – 1656.3, with the identification of peaks that indicate the mineralogy.

The XRD analysis of the clay fraction showed similar relationships among the samples as seen in the bulk analysis, with six being nearly identical (DCC – 1656.3, DCC – 1668.5, DCC – 1668.7, DCC 1668.9, DCC – 1677.3, and DCC – 1675.2) and the seventh sample showing different results (DCC – 1641.5). The data show no noticeable differences in the diffractograms between the 2-16 micron and less than 2 micron fractions, except in peak intensity, which can be attributed to mineral concentrations being lower overall in the less than 2 micron fraction (Moore and Reynolds, 1997) (Figures 4.12 and 4.13). The peaks at 2θ values ~6.5 and ~8 degrees indicate that

chlorite and illite are the primary clay minerals present in these samples, respectively. The diffractogram for Sample 1641.5 shows only a small peak at ~8 degrees, meaning illite is present and chlorite is not, but only in small concentrations based on the peak intensity (Figure 4.14). The diffractograms for the clay fraction samples exposed to the glycol treatment (Figures 4.15 and 4.16) display no changes, compared to the diffractograms of the samples before exposure, except in sample DCC – 1641.5. Figure 4.17 displays the diffractograms of sample DCC – 1656.3 from before and after the glycol treatment and is representative of all the samples, except for DCC - 1641.5. In sample DCC - 1641.5, there is a peak at the 2θ value of ~32 degrees in the non-treated sample that is not seen after the exposure to the glycol treatment (Figure 4.14).

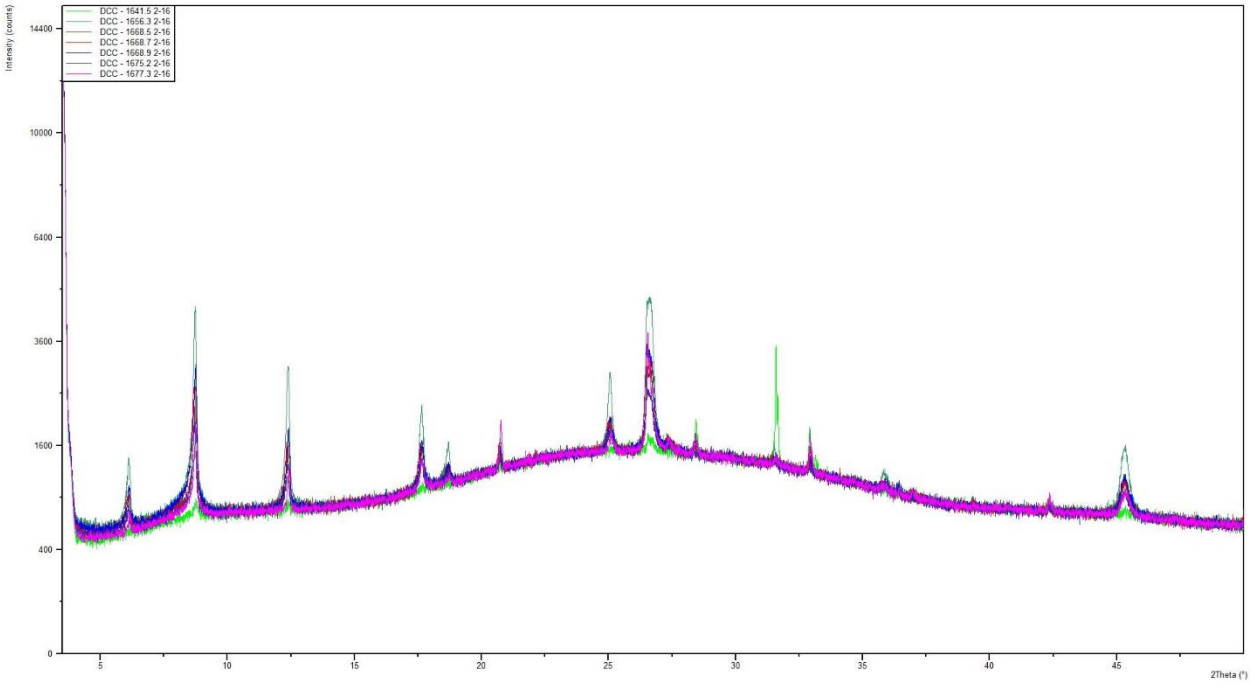

Figure 4.12: Diffractograms for all seven clay fraction samples (2-16 Microns).

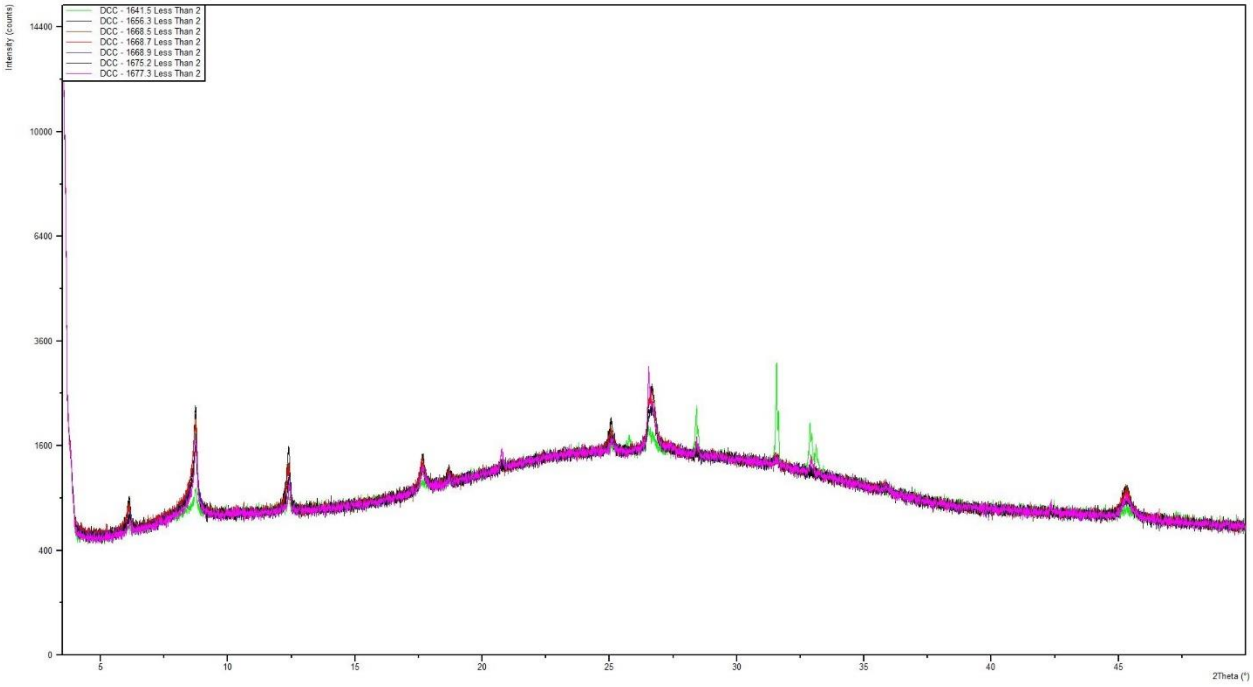

Figure 4.13: Diffractograms for all seven clay fraction samples (less than 2 microns).

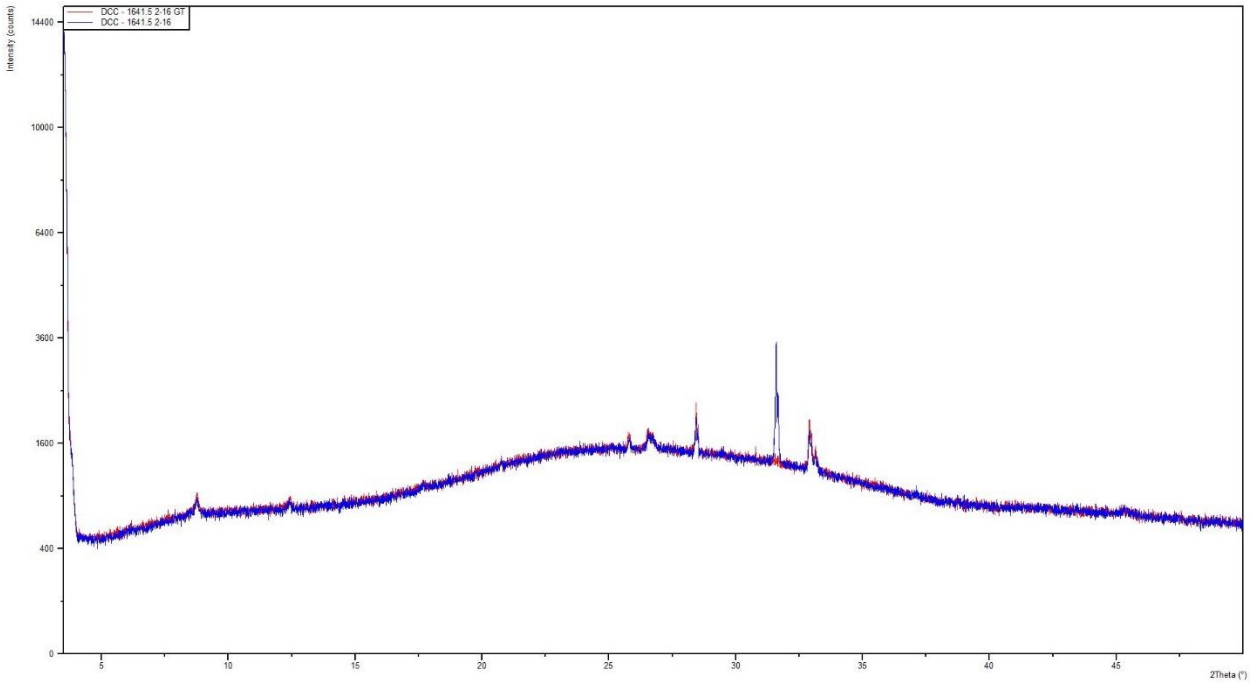

Figure 4.14: Diffractograms for Sample DCC – 1641.5 before (blue) and after (red) exposure to the glycol treatment (2-16 microns).

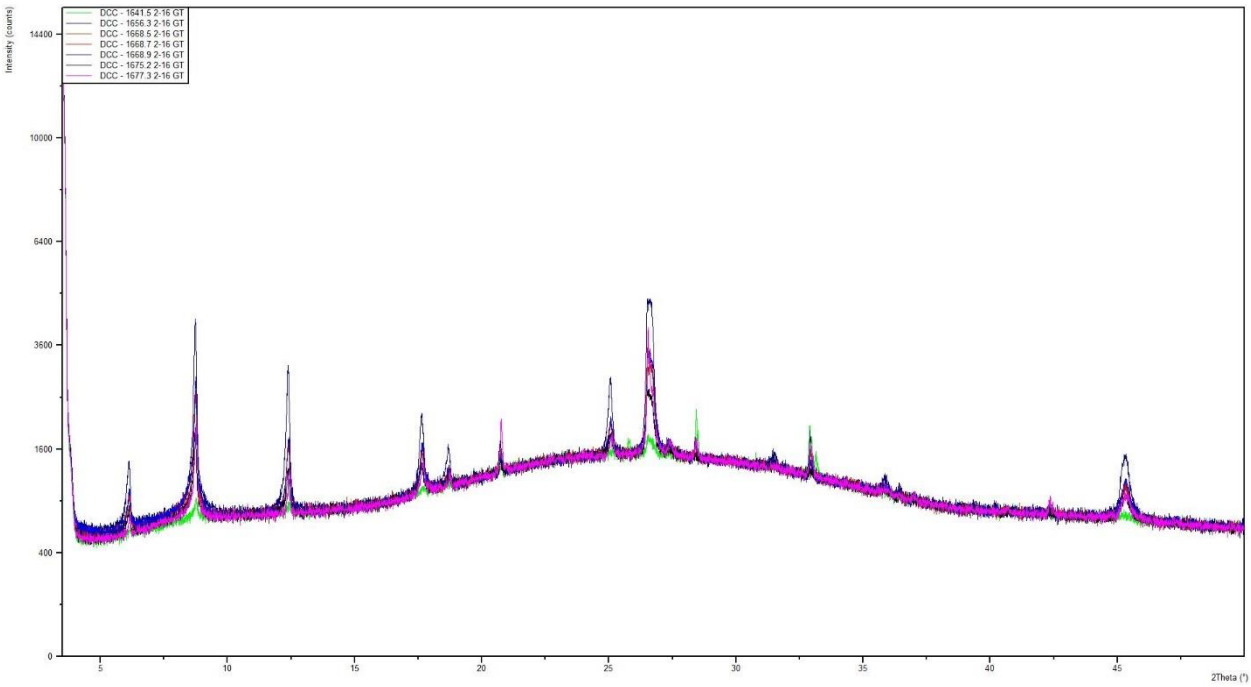

Figure 4.15: Diffractograms for all seven clay fraction samples after exposure to the glycol treatment (2-16 microns).

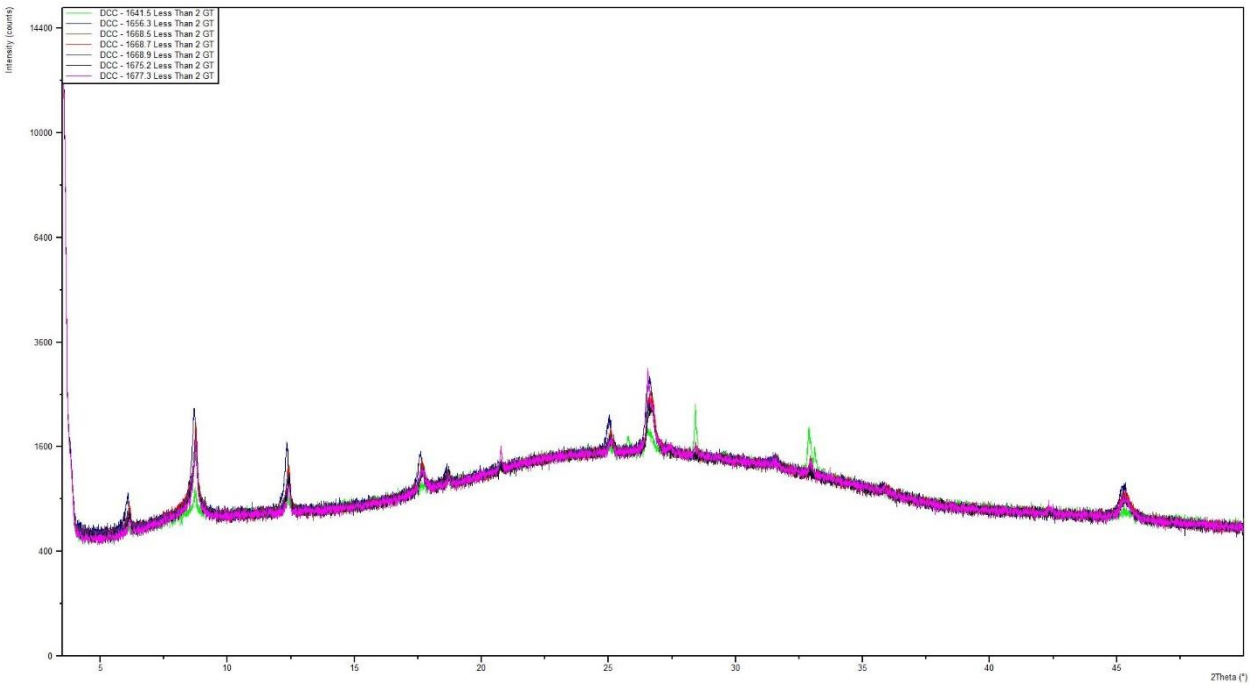

Figure 4.16: Diffractograms for all seven clay fraction samples after their exposure to the glycol treatment (less than 2 microns).

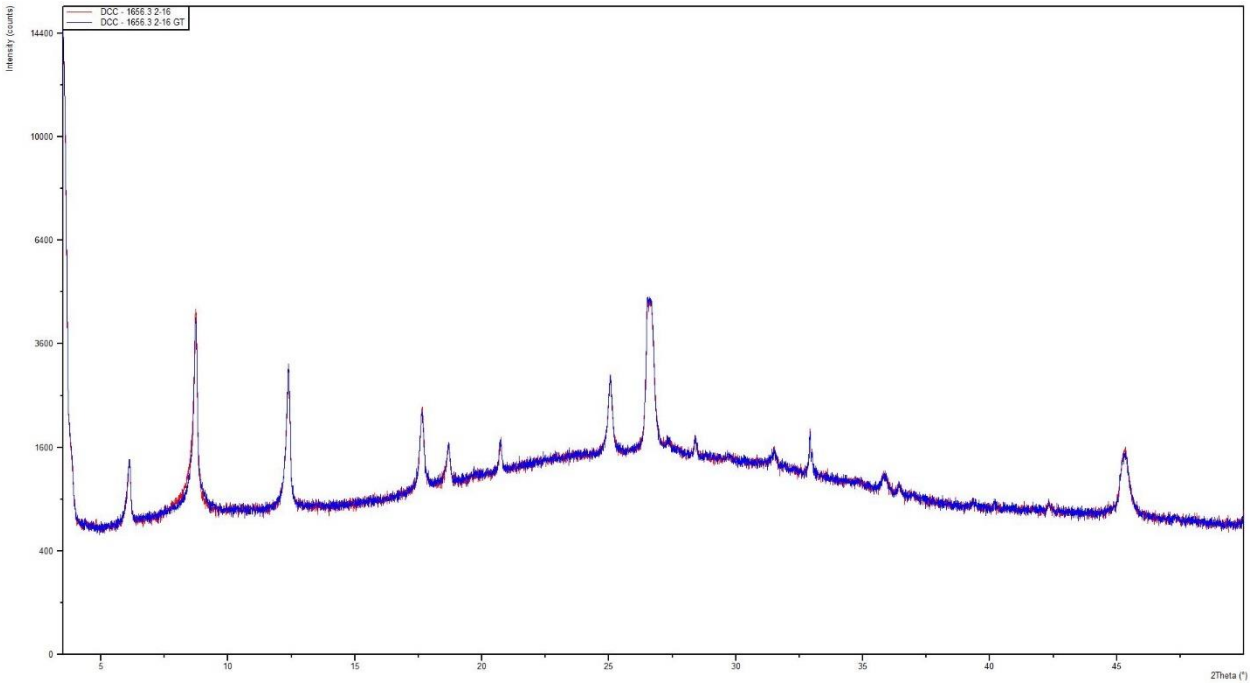

Figure 4.17: Diffractograms for Sample DCC – 1656.3 before and after the exposure to the glycol treatment (2-16 microns).

Geochemical analyses

The raw data for the elemental concentrations collected with the HHXRF can be seen in Appendix A. These data were used to construct the chemostratigraphic logs displayed in Figure 4.1.

The analysis of the chemostratigraphic signatures allowed the identification of three distinct sections in the study core. The limit between these zones coincides with facies boundaries and will be discussed below. The lowermost section (Sequence 1) ranges from 1678 to 1665 ft deep. The middle section (Sequence 2) is located between 1665 and 1647 ft deep, and the topmost section (Sequence 3), between 1647 and 1638.5 ft deep.

Sequences 1 and 3 are characterized by higher variation in detrital input proxies (Ti/Al, Zr/Al, and Si/Al), some of the anoxia proxies (Ni/Al and Mo/Al) and P/Al (a productivity proxy), while Sequence 2 shows little to no variation in these proxies.

All three detrital input proxies are tightly correlated, displaying the same peaks across these logs.

P/Al, a primary productivity proxy, coincides with the detrital input proxies, except for one major peak at 1648 feet that is not seen in the detrital proxies, but is present in the anoxia proxies. The other primary productivity index, Ba/Al, shows consistent variation in the entire core, without significant peaks or signatures that could be used for breaking the succession.

The anoxia proxies (Cu/Al, Fe/Al, Mo/Al, Ni/Al and Zn/Al) can be subdivided into two groups. The first group (Cu/Al, Fe/Al, and Zn/Al) show the same overall trends, with little variation throughout the length of the core (except for a few, small peaks). The second (Ni/Al and Mo/Al) display different signatures in the three sections of the core (more variable in Sequences 1 and 3).

The ICP-MS data can be seen in Table 4.2. The absolute elemental concentrations from the ICP-MS data do not compare directly with the concentrations gathered by the HHXRF due to the limitations of HHXRF in terms of precision and accuracy. However, an agreement in the relative elemental concentrations obtained from the two methods would nonetheless secure the ability to use those for interpretation of the depositional processes. To evaluate how well the HHXRF captured the variation in elemental concentration in comparison with ICP-MS, elemental concentration data for individual elements obtained from both analytical methods were plotted against each other (Figures 4.18 and 4.19), with the expectation that a good correlation would display a high degree of confidence in the concentrations obtained with HHXRF. Mo, Ba, and Zr were used as tests to examine the validity of the quantitative results from the HHXRF data.

The strength of the correlation between the ICP-MS and HHXRF data varies from element to element. The Mo data shows an R^2 correlation of 0.3744. Six of the ten data points follow the

trend closely, while the remaining four do not. Ba, with an R^2 value of 0.376, is nearly the same, with seven of the ten data points lying near the trendline. The Zr plot has an R^2 correlation of 0.9507.

The R^2 values for Ba and Mo are relatively low values, with the correlations drawn down significantly by a few points (Figure 4.19). The reduced number of samples also decrease the statistical significance. The high R^2 values for Zr provides good confidence for the elemental concentrations obtained with HHXRF for this element. The large discrepancy between the correlations for Mo in comparison with Zr is probably related to their absolute concentrations in the studied rocks, since Mo concentrations are typically a few parts per million (< 10 ppm), whereas Zr concentration is typically a few hundreds of ppm (150-200 ppm).

ICP-MS Data from Douglas County Core Samples														
Sample ID	**Mo ppm**	**La ppm**	**Ce ppm**	**Pr ppm**	**Nd ppm**	**Sm ppm**	**Eu ppm**	**Gd ppm**	**Tb ppm**	**Dy ppm**	**Ho ppm**	**Er ppm**	**Tm ppm**	**Yb ppm**
KGO Woodford std	16.28915	19.01715	37.04046	4.37991	16.08187	3.20613	0.66682	2.81692	0.46076	2.76090	0.56218	1.52027	0.22180	1.36397
DCC-1638.5	1.44121	23.55919	46.95882	4.61298	15.74050	2.81498	0.57454	2.23411	0.41049	2.87582	0.63595	1.92503	0.31150	2.04335
DCC-1643	3.53783	40.54777	80.03912	8.95756	30.30352	4.47876	0.85972	3.07460	0.58003	3.89621	0.82891	2.54416	0.38654	2.58440
DCC-1645	2.08599	39.93842	81.38249	9.05282	31.92696	5.89037	1.17652	4.85958	0.84053	5.34478	1.11042	3.10562	0.46012	2.92204
DCC-1648	14.52194	37.03842	71.92054	8.77937	31.15570	5.30654	1.02438	3.84558	0.65914	4.22486	0.87558	2.51883	0.39101	2.48298
DCC-1651	1.88103	37.24523	71.93842	8.70410	31.29991	5.46327	1.08363	4.19125	0.71542	4.52210	0.94198	2.61919	0.39565	2.57387
DCC-1655	15.52159	36.75142	70.25184	8.60993	31.56273	5.90267	1.15168	4.50603	0.74907	4.66974	0.95129	2.69618	0.40857	2.56763
DCC-1666	8.20195	36.47133	73.00814	8.90224	32.59064	6.06513	1.15858	4.56363	0.77934	4.66249	0.96856	2.67815	0.40893	2.58708
DCC-1667	10.50034	38.50434	79.63465	9.37747	35.89859	8.41664	1.66819	7.15477	1.07506	6.13704	1.21421	3.24138	0.48336	3.03014
DCC-1674	17.81593	37.23881	74.83979	8.86368	32.58672	6.58657	1.27923	5.24928	0.86313	5.31316	1.07530	2.94498	0.44621	2.78913
DCC-1676.5	5.56261	37.53674	71.80268	8.16440	27.80554	4.46547	0.82097	2.97357	0.54289	3.62424	0.79840	2.36055	0.36491	2.46979
DCC-1639	1.27347	23.24056	46.36356	4.57762	15.59529	2.82210	0.56735	2.21388	0.40837	2.75167	0.61125	1.91078	0.30235	1.99132

Sample ID	**Lu ppm**	**Ba ppm**	**Th ppm**	**Nb ppm**	**Y ppm**	**Hf ppm**	**Ta ppm**	**U ppm**	**Pb ppm**	**Rb ppm**	**Cs ppm**	**Sr ppm**	**Sc ppm**	**Zr ppm**
KGO Woodford std	0.20933	193.67890	5.61671	7.74268	14.85637	2.48129	0.55366	9.94352	17.68051	72.36670	4.45799	233.53476	7.82448	92.78593
DCC-1638.5	0.33535	231.99318	13.17438	16.03414	16.24674	4.55317	1.06534	3.39302	17.83651	206.04091	16.57303	76.56475	18.89317	164.76977
DCC-1643	0.39452	540.74563	11.82021	14.09777	21.26393	3.73811	1.01077	3.74707	9.54708	226.54203	12.24286	98.91950	20.93530	133.15239
DCC-1645	0.45849	364.03053	11.37145	13.49407	29.35623	4.75039	0.95797	3.95713	12.77126	167.31108	9.15246	113.40225	15.33021	171.60213
DCC-1648	0.38774	526.95311	10.80224	12.79289	21.46217	3.38577	0.91809	4.78263	13.26783	216.18898	11.69155	96.04024	20.59976	120.25259
DCC-1651	0.39296	518.08404	10.92026	12.99223	23.69234	3.67113	0.93752	3.45653	10.17961	212.56278	11.45889	99.89961	20.12164	130.76376
DCC-1655	0.40229	533.43075	11.02736	12.93287	24.40132	3.51306	0.93019	5.22673	18.20008	220.06576	12.31794	110.64388	20.60135	123.09866
DCC-1666	0.40422	489.43873	12.11943	14.03656	23.26958	3.86185	1.02525	3.74080	21.86227	201.86081	11.64729	106.13519	18.45832	136.14727
DCC-1667	0.46013	446.17442	11.44262	14.65797	30.49832	4.91411	1.06059	4.33911	22.29141	185.60046	10.16191	103.32207	17.84930	175.40668
DCC-1674	0.44751	457.11413	12.08097	13.46990	26.08201	4.11671	0.97499	6.86477	28.83433	200.24575	11.58060	101.76114	19.10130	146.47098
DCC-1676.5	0.38319	507.71288	11.26082	13.61926	19.31874	3.67469	0.98452	4.52965	20.88523	219.34174	12.25039	107.62535	20.57839	128.95676
DCC-1639	0.32498	229.46879	12.96783	15.75199	15.77884	4.48486	1.05322	3.29180	17.19458	203.24164	16.34383	74.28829	18.38698	165.65330

Table 4.2: ICP-MS data from 10 samples in the Douglas County core.

It is important to also consider that the precision and accuracy of these two analytical methods are not the only possible reasons for the discrepancies in their results. The HHXRF only measures data at an individual point on the sample. This means that, by taking a measurement at the same depth in the core, but in a slightly different, lateral location, the results would be slightly different. It is also possible that the point selected for the HHXRF analysis was influenced by a larger clast in the measurement that is not truly representative of the bulk rock at that depth. The ICP-MS data is generated from the analysis of homogeneous shale samples that likely to represent an average of the actual composition of the rock at those specific depths.

In any case, the HHXRF is capable of providing valuable data for certain elements, if not quantitatively, at least qualitatively.

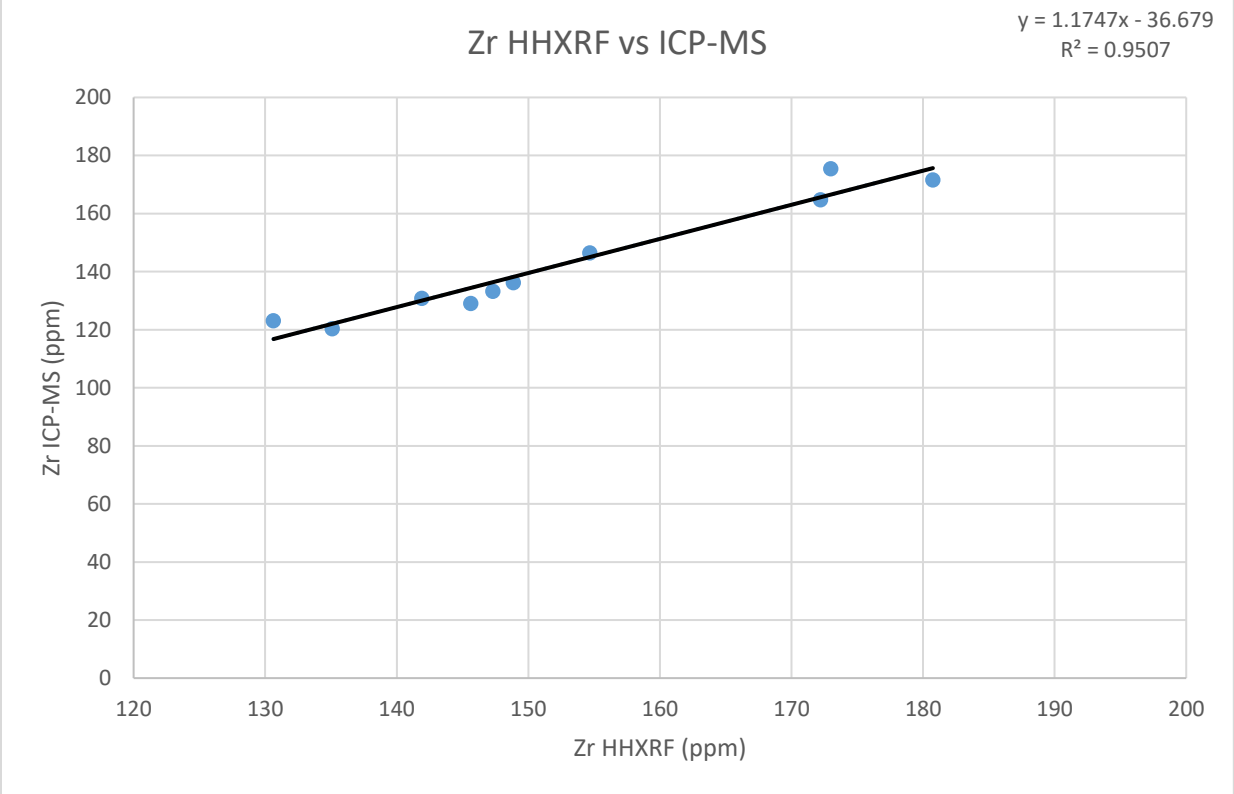

Figure 4.18: Cross plots of ICP-MS and HHXRF data showing the correlation of Zr concentrations.

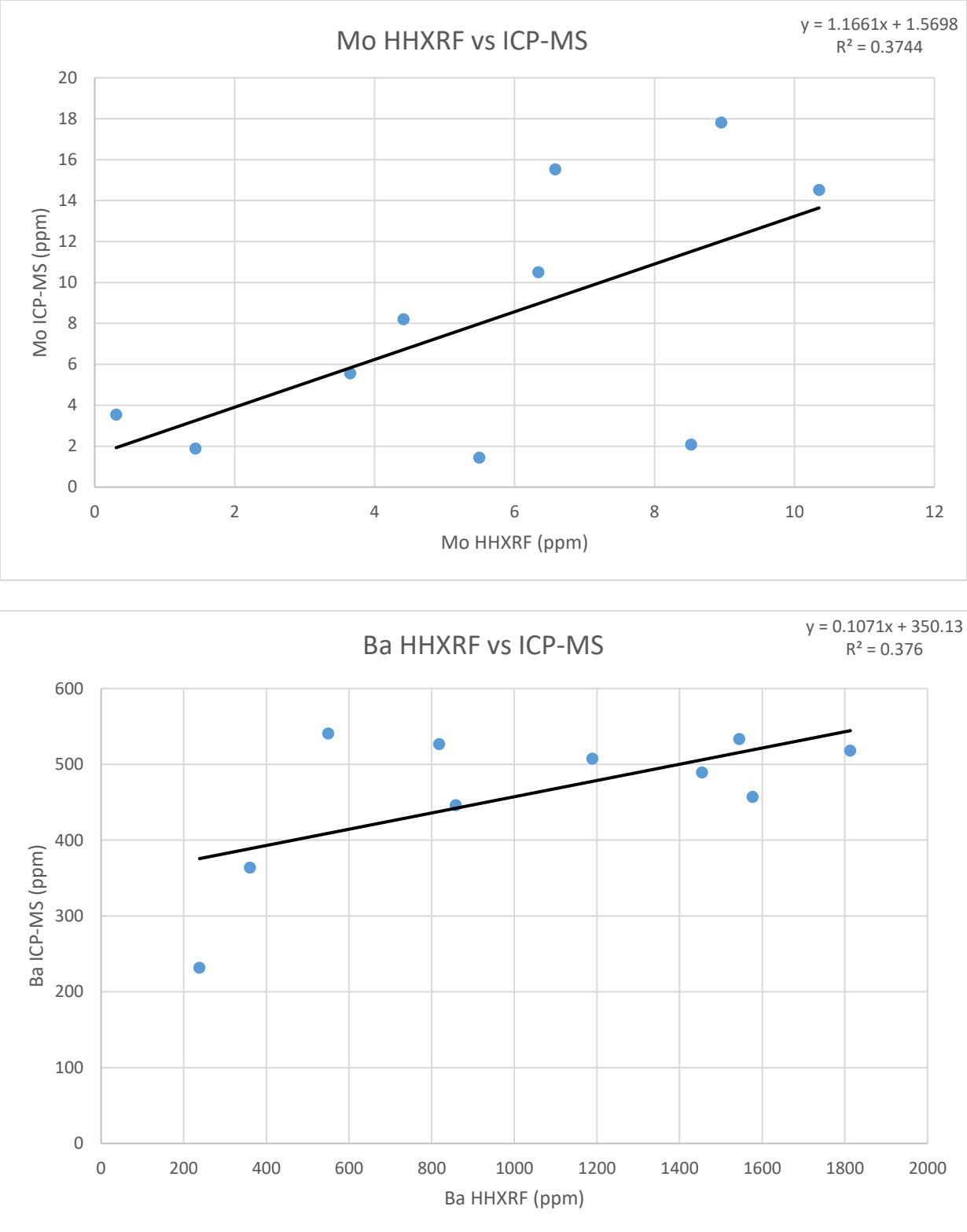

Figure 4.19: Cross plots of ICP-MS and HHXRF data showing the correlation between Mo and Ba concentrations

ICP-MS analysis was essential to check the Mo and to obtain U concentrations, the latter of which cannot be not obtained by HHXRF at low concentrations.

Enrichment factors (EF) calculated for the different redox-sensitive elements (Zn/Al, Ni/Al, U/Al, Mo/Al, Cu/Al and Co/Al) are displayed in two logs due to scale differences, to ensure that the subtle changes in EFs can be easily seen (Figures 4.20 and 4.21). The portions of the logs to the left of the "line of enrichment" (EF = 1) have lower concentrations of the specific element than average shale (i.e. is depleted in relation to the average shale), whereas the portions that lie to the right of the "line of enrichment" represent elemental concentrations greater than the average shale (i.e. enriched). The EF for U is plotted as data points at the depth where the samples analyzed by ICP-MS where collected.

Through nearly the entirety of the core, Mo is strongly enriched in relation to average shale. The few data points obtained by ICP-MS analysis show the U is consistently enriched in the Chattanooga Formation. The opposite is true for Cu and Ni, consistently depleted or equivalent to average shale. Co shows some isolated peaks of enrichment throughout the core, and Zn is mostly depleted, except for some isolated peaks in Sequences 1 and 2. Sequence 3 is clearly more enriched in Zn.

The TOC and sulfur results are provided in Table 4.3. TOC in the ten samples analyzed is not high, relative to average Chattanooga TOC measurements from Comer and Hinch, (1987), with all but two samples with TOC less than 1% (0.16-0.985 wt%) . Sample 1674 ft has TOC equals to 3.43 wt%, and sample 1666 ft, 1.67 wt%. Both are located in Sequence 1. Sulfur is not particularly high in most samples, ranging from 0.34 to 0.86% in Sequences 2 and 3. In Sequence 1, however, the three samples show high S content (1.76-4.61%).

The meaning of these variations and the controls on the accumulation of organic matter in fine-grained sediments will be discussed in Chapter 5.

LECO C/S Data			
Sample ID	**Depth (ft)**	**TOC (wt%)**	**% Sulfur**
DCC-1638.5	1638.5	0.244	0.52
DCC-1643	1643	0.16	0.34
DCC-1645	1645	0.21	0.71
DCC-1648	1648	0.74	0.76
DCC-1651	1651	0.463	0.86
DCC-1655	1655	0.985	0.84
DCC-1666	1666	1.67	1.76
DCC-1667	1667	0.19	4.61
DCC-1674	1674	3.43	2.03
DCC-1676.5	1676.33	0.306	2.2

Table 4.3: TOC and sulfur data from Douglas County core samples.

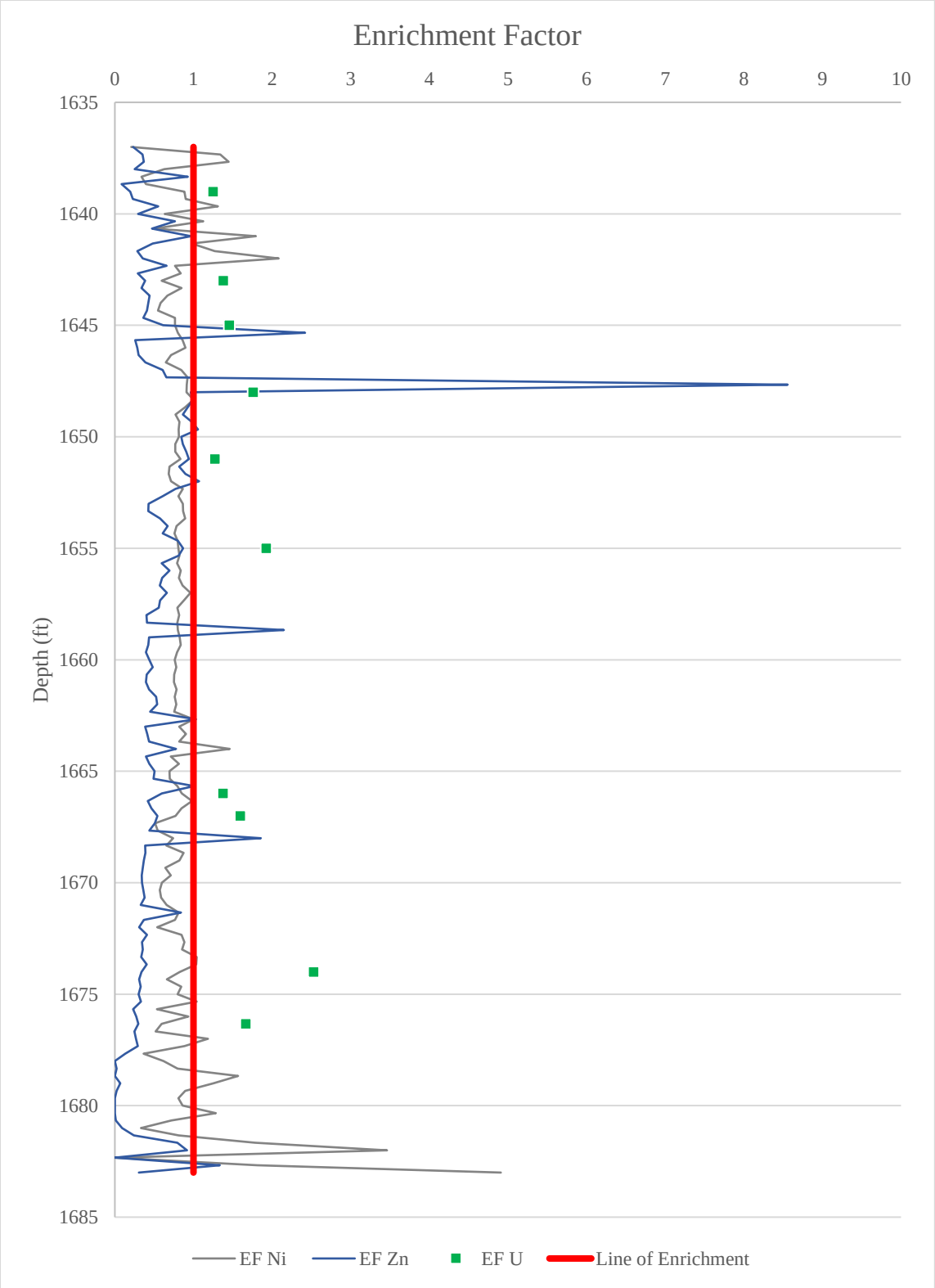

Figure 4.20: Logs displaying the enrichment factors (EFs) for Ni, Zn and U calculated from HHXRF (Ni and Zn) and ICPMS (U) data along the study core. The "Line of Enrichment" limits depleted values (below) from enriched values (above).

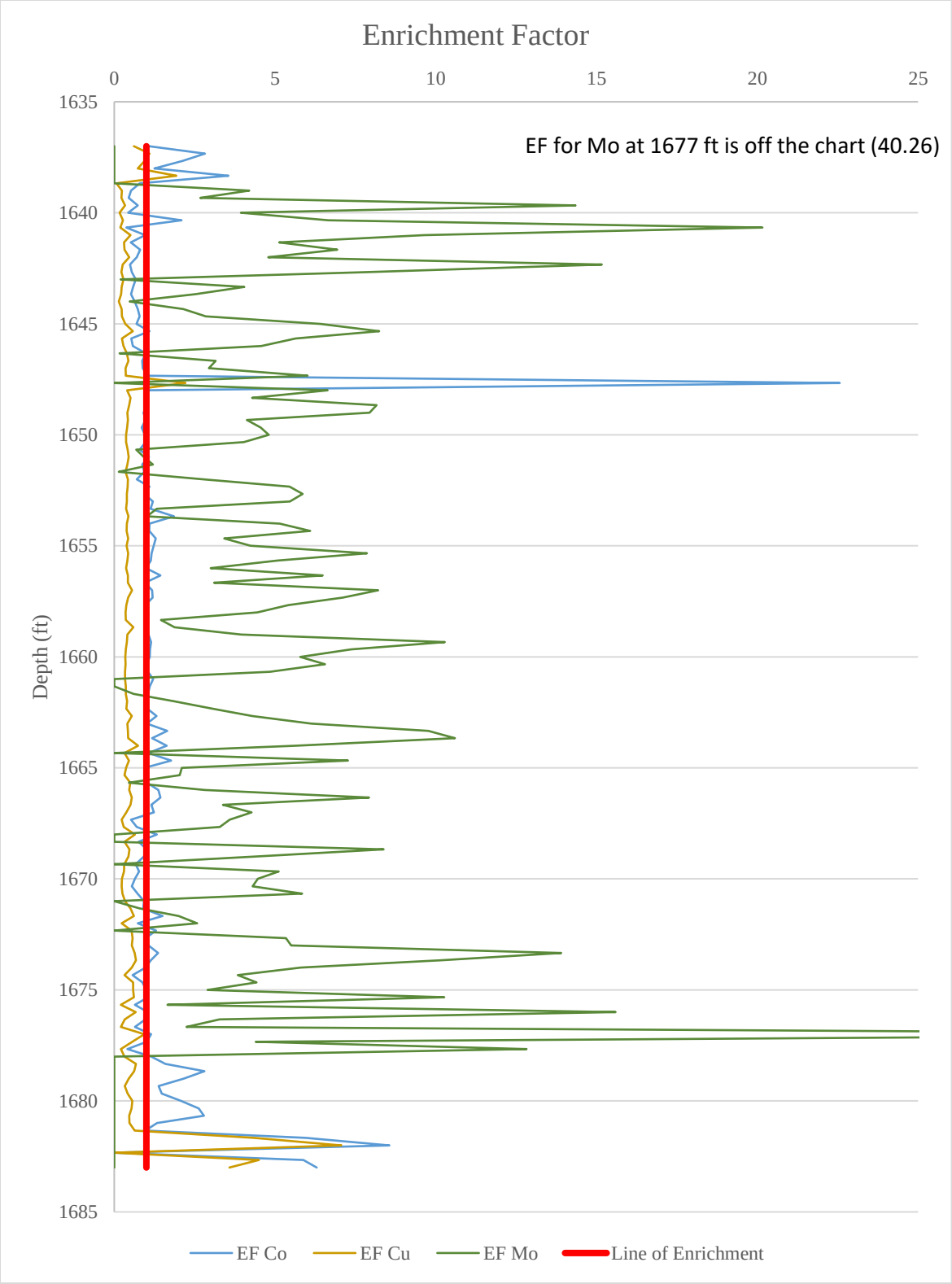

Figure 4.21: Logs displaying the enrichment factors (EFs) for Co, Cu and Mo calculated from HHXRF data along the study core. The "Line of Enrichment" limits depleted values (below) from enriched values (above).

Cross-Correlation Through Wavelet Transform

The cross-correlation performed between indices used as proxies for detrital input (Ti/Al, Zr/Al, Si/Al) can be seen in Figure 4.22. In this figure, warmer colors (i.e. higher degree of correlation) are focused in three separate areas, between 1640-1650 ft, ~ 1664 ft, and ~ 1676 ft. These correlations are seen at intervals that range from less than a foot, up to ~ 2 feet.

For the productivity indices (P/Zn, Cu/Al, Zn/Al), the results are similar to the detrital input proxies (Figure 4.23). There are three main areas where warmer colors occur, at scales that range from less than a foot to ~2 feet. These sections are at depths 1655-1650 ft, ~ 1664 ft, and ~ 1676 ft.

Cross-correlation using the wavelet transform method in MATLAB applied to the Chattanooga Formation indicates that, at the same depths, the detrital input and the productivity indices are more strongly correlated.

Although the goal of this method was to detect correlations that may be missed by human examination, all the correlations determined by this method for this particular data set coincide with the key peaks in these indices in Figure 4.1. Therefore, although the method did accurately find correlations between the data put into the MATLAB code, it did not detect correlations on a finer scale. Perhaps the application of this method to a dataset collected with a finer sample resolution (i.e. every inch, rather than every four inches) could allow for the detection of correlations in higher resolution, if present.

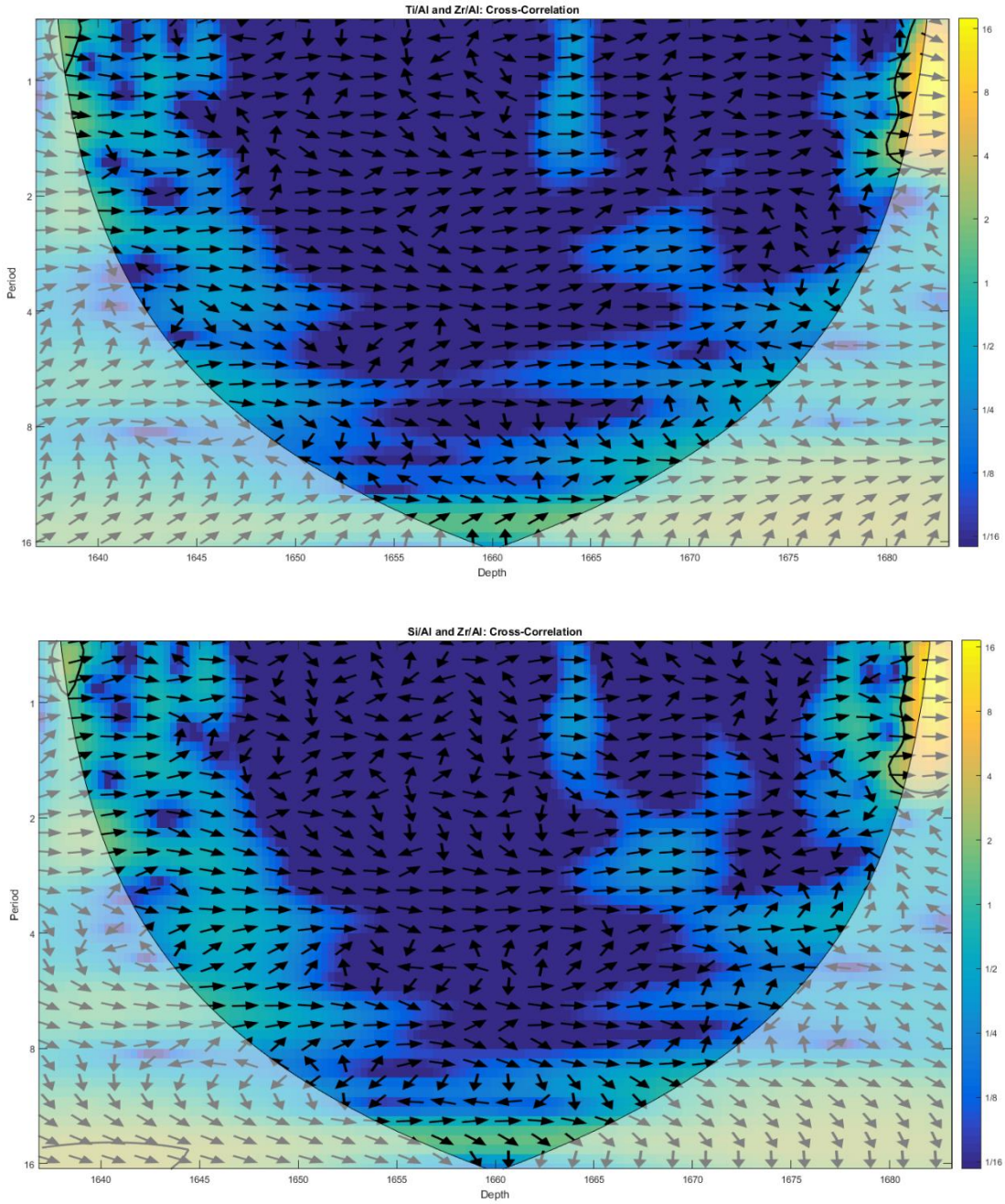

Figure 4.22: Plots showing the cross correlations between detrital input proxies, Ti/Al and Zr/Al (top panel) and Si/Al and Zr/Al (bottom panel), calculated using the wavelet transform method in MATLAB. The x axis is core depth (in feet, increasing to the right), and the y axis is the period. The color scale represents the degree of correlation.

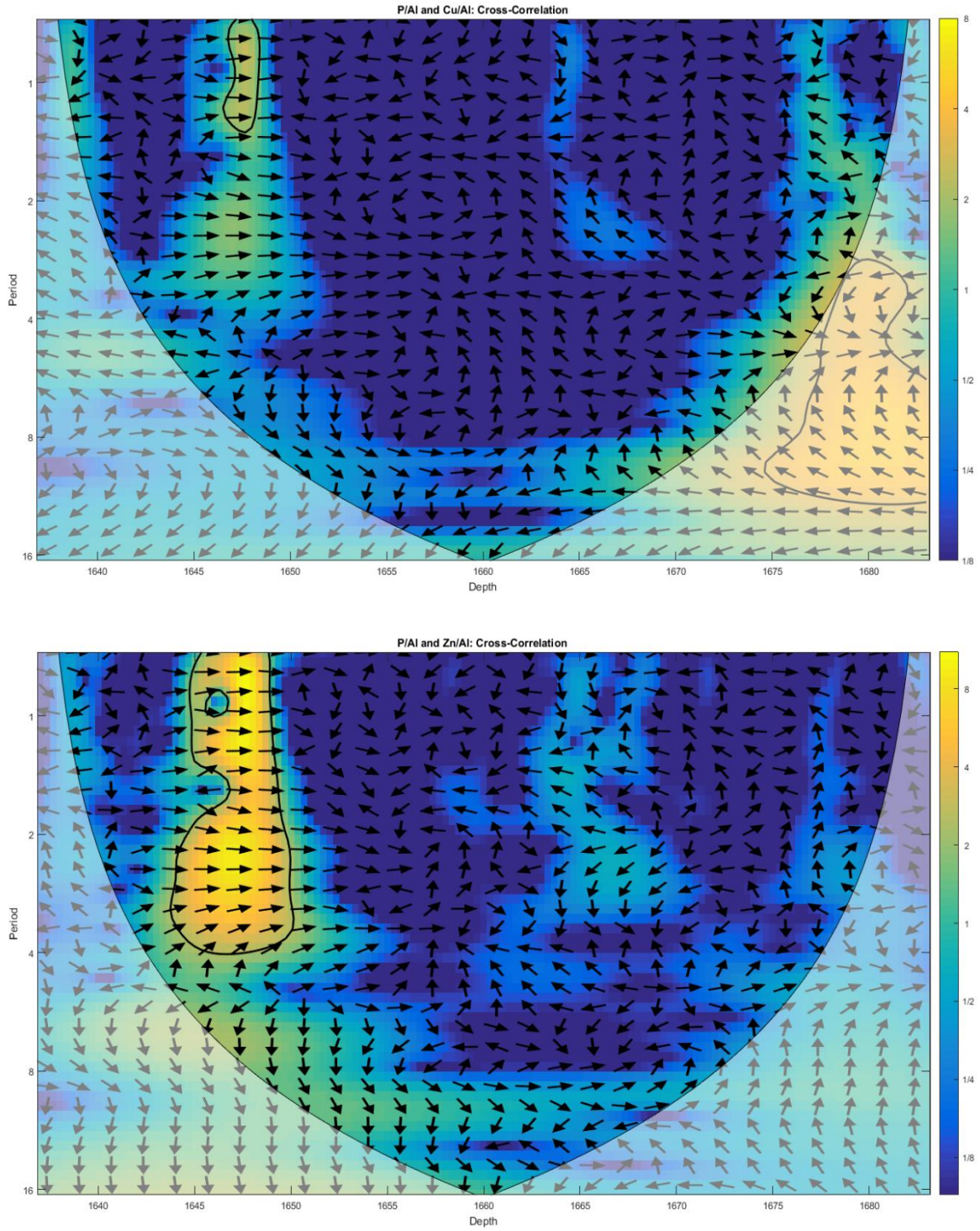

Figure 4.23: Plots showing the cross correlations between detrital input proxies, P/Al and Cu/Al (top panel) and P/Al and Zn/Al (bottom panel), calculated using the wavelet transform method in MATLAB. The x axis is core depth (in feet, increasing to the right), and the y axis is the period. The color scale represents the degree of correlation.

Chapter 5 - Discussion

The sedimentological and chemostratigraphic analyses of the Chattanooga Formation in the study core showed that the sedimentary succession can be divided in three units (from base to top, Sequences 1 through 3) (Figure 4.1), based on their vertical facies associations and certain chemostratigraphic indices. Not all indices were useful in distinguishing the sequences. The most useful ones were the proxies for detrital input (Ti/Al, Zr/Al and Si/Al), P/Al (proxy for primary productivity) and Ni/Al and Mo/Al (proxies for anoxia). Ba/Al showed little variation throughout the entire Chattanooga Formation, with no signature typical of one or another sequence, and hence was not used to differentiate the sequences in terms of primary productivity. Cu/Al, Fe/Al and Zn/Al are nearly constant for the entire length of the core, and therefore of limited use in distinguishing different sequences. The little variation in Cu/Al and Zn/Al may be a result of limited amounts of H_2S available in the seawater to precipitate out copper and zinc as sulfides (Calvert and Pedersen, 1993). Constant, low Fe/Al is probably related to deposition of the Chattanooga Formation under anoxic conditions, since Fe would remain in solution rather than precipitated as oxides (Calvert and Pedersen, 1993).

The sequences identified in this study are roughly equivalent to the informal members (lower, middle and upper) proposed by Ellison (1950) and Comer (1991) on the basis of geophysical logs, and the transgressive and highstand systems tracts defined for the Woodford Formation in Oklahoma by Turner et al. (2016). In this work these units have been interpreted as depositional sequences, as detailed below.

Sequence 1 (depth 1678 to 1665 ft) is characterized by frequent facies changes dominated by fMs-2 and fMs-5, with the intermittent occurrences of fMs-1, fMs-4 and cSs. This sequence contains phytoclasts, AOM and *Tasmanites*. Given the dominant facies and type or organic matter,

the deposition of Sequence 1 was influenced by periods of high detrital input, possibly resulting from current and/or wave action that reworked and oxygenated the bottom. These frequent, short-lived "aeration events" led to the establishment of an environment that alternated between oxic to nearly anoxic conditions in high frequency. The chemostratigraphic signature of detrital input indices, primarily Ti/Al, show the same pattern, with peaks representing enhanced detrital input (Sageman and Lyons, 2004; Bhatia and Crook, 1986; Pearce and Jarvis, 1992; Pearce et al., 1999; Sageman and Lyons, 2004).

Sequence 1 displays highly variable P/Al, suggesting highly variable primary productivity (Tribovillard et al., 2006). Phosphate is common in deep water and is a main nutrient for microscopic life, so when brought to the surface through upwelling, for example, it can trigger productivity blooms (Berger et al., 1994). Increased organic flux can also result from riverine nutrient input. Regardless of the nutrient-delivery agent, anoxia can be a consequence of increased organic flux (Gallego-Torres et al., 2007; Berrocoso et al., 2010). These fluctuations in primary productivity could also be a cause for cyclicity in the degree of oxygenation. Under high organic fluxes, microbial decomposition of the organic carbon results in anoxia; hence high-frequency variations in the organic flux may account for the frequent interbedding of oxic and more anoxic facies and the variable P/Al in Sequence 1. Likewise, Mo/Al and Ni/Al are highly variable, suggesting frequent variations in the degree of oxygenation.

Relative to average shale, Sequence 1 is enriched in Mo and U, partially enriched in Co, and depleted in Cu, Ni, and Zn. The enrichment in Mo and U indicates deposition under anoxic conditions. Cu, Ni and Zn are trace metals that are used as paleoproductivity proxies (Tribovillard et al., 2006). Their depletion suggests that the overall amount of organic material in this section

was low, which agrees with the TOC data in Sequence 1. The highest TOC values in the study core, however, were found locally in this sequence.

The integration of sedimentological and chemostratigraphic data in Sequence 1 points to a scenario of dominantly anoxic conditions, with frequent pulses of sediment reworking that supplied siliciclastic sediments, terrestrial organic matter, and oxygen to the bottom waters. It is possible that riverine input delivered nutrients that increased primary productivity.

Sequence 2 (depth 1665 to 1647 ft) is dominated by facies fMs-5, fMs-4, and fMs-1, subordinately fMs-3. Each individual facies occurs as thick successions, attesting to the constancy of the depositional conditions. The organic matter types in these facies include mostly AOM and *Tasmanites*, and trace amounts of phytoclasts. This sequence shows relatively low and constant chemostratigraphic indices, meaning that, during its deposition, detrital input and primary productivity were constantly low, and the degree of oxygenation was also constant. These and the thick lithofacies suggest that Sequence 2 was formed during longer-lived anoxic cycles. While during the deposition of Sequence 1 the degree of oxygenation fluctuated frequently, during the deposition of Sequence 2 the depositional conditions remained unchanged for long periods of time, mostly with low oxygen levels, based on the enrichment in Mo and U. The scarcity of phytoclasts and the low detrital input suggests that riverine input was insignificant during the deposition of Sequence 2, possibly reflecting an increase in water depth. A low-productivity setting is suggested by the proxies, in agreement with the low TOC values.

Sequence 3 (depth 1647 to 1638.5 ft) contains dominantly facies fMs-6, subordinately fMs-2 and fMs-3, and rarely fMs-1; it is the only sequence with the diagenetic facies cMs and mMs. Facies shifts in this sequence are more frequent than in Sequence 2, but not as frequent as in Sequence 1. The organic matter present include phytoclasts, AOM, *Tasmanites*. The facies

associations suggest that the degree of oxygenation varied from sub-oxic to anoxic. The chemostratigraphic data display high, variable Ti/Al, Zr/Al and Si/Al ratios, indicating increases in detrital input at the time of deposition. Increases in P/Al, and Ni/Al and Mo/Al point to increased primary productivity and anoxia, respectively.

Sequence 3 is also enriched in Mo and U, locally enriched in Co and Ni, and depleted in Zn and Cu. The enrichment in Mo and U points to deposition under anoxic conditions. Similar to Sequence 1, the depositional setting during the deposition of Sequence 3 seems to have been dominantly anoxic, with pulses of increased siliciclastic input that also brought in terrestrial organic matter. In contrast to Sequence 1, however, in Sequence 3 the enrichment in Co and Zn point to a high-productivity setting. It is likely that high productivity driven by riverine nutrient input (increasing the organic flux), associated with persistently anoxic conditions (favoring the preservation of organics), are the controlling factors in Sequence 3.

The occurrence of diagenetic facies in Sequence 3 is probably due to remobilization of carbonate-rich fluids derived from the overlying carbonates during diagenesis.

Despite the apparent homogeneity of the Chattanooga Formation, the numerous facies and chemostratigraphic changes detected in this unit were formed in response to changes in several controls, most importantly detrital input and primary productivity. In Sequences 1 and 3, oxygenation cycles seem to have been driven by variations in primary productivity, which in turn were driven by variations in detrital input. In Sequence 2, however, the low detrital input and suboxic-anoxic conditions may have been driven by an increase in water depth, perhaps reflecting higher sea levels. Sequence 3 possibly reflects the conjunction of increased primary productivity and persistent anoxia, due to high sea level, that led to increased organic flux and preservation in the sediments.

Chapter 6 - Conclusions

An integrated sedimentologic-chemostratigraphic study of the Chattanooga Formation in Kansas has led to the following conclusions.

The sedimentary succession comprises nine facies, seven depositional and two diagenetic. For the depositional facies, the majority are fine mudstones. Attributes such as type of organic matter and degree of bioturbation were used to determine the proximity relative to the shoreline. The two coarser-grained depositional facies are cSs and mMs, the fine-grained facies are fMs-1 through fMs-6. The diagenetic facies are cMs and mMs.

Overall the mudstones consist of quartz, muscovite, chlorite, illite, pyrite, and one sample contains calcite. Variable proportions of different types of organic matter (phytoclasts, AOM and *Tasmanites*) were found in the mudstones, reflecting differences in terrestrial and algal contributions. The overall concentrations of organic carbon were low: most of the samples had less than 1% TOC. The few organic-rich samples (give range for what you view as organic rich) were found in Sequence 1.

Three sequences were defined on the basis of facies associations and chemostratigraphic signatures, and the boundaries show similarities to boundaries defined in previous work (Ellison 1950). The first sequence showed relatively rapid changes between multiple facies during deposition. The chemostratigraphic logs, in general, show frequent variations with depth for all of the investigated proxies, which were interpreted as the result of variations in detrital input, primary productivity and anoxic conditions. Sequence 2 was more homogeneous throughout. All of the indices were low and showed limited variation, reflecting a relatively constant, low detrital input and primary productivity, combined with longer-lived oxygenation cycles and suboxic-anoxic conditions during deposition. Sequence 3 is more similar to Sequence 1, exhibiting frequent facies

and chemostratigraphic changes and evidence for greater detrital input. The main difference between Sequence 1 and Sequence 3 is that Sequence 3 possibly reflects increased primary productivity and persistent anoxia that led to higher organic flux and preservation in the sediments, which makes it the most favorable sequence for the accumulation of organics in the sediments.

Chemostratigraphic logs and the wavelet transform method were useful in identifying the large-scale sequences, but were not refined enough to subdivide the sequences into systems tracts. With chemostratigraphic data collected at a finer resolution, perhaps every 1 inch rather than every 4 inches, maybe smaller scale cycles could have been detected.

The best proxies to assess the controls on the accumulation of organic matter in the sediments were Ti/Al, Zr/Al and Si/Al for detrital input, P/Al for primary productivity and Mo/Al and Ni/Al for anoxia, which clearly differentiate the three sequences.

This study on the Chattanooga Formation suggest that the main control in the accumulation of organic matter in these sediments was primary productivity. In most instances, anoxia seemed to have been driven by the high organic flux. However, the most favorable condition for the formation of organic-rich sediments is when high organic flux is accompanied by anoxia (due to increasing water depth), such as in Sequence 3.

References

Barrick, J. E., J. N. Haywa-Branch, and D. J. Over, 1990, Stop 6: Woodford Shale (Late Devonian-Early Mississippian), pre-Weldon Shale, Weldon Limestone, and basal Caney Shale (Mississippian); Hass G section, in S. M. Ritter, ed., Early and middle Paleozoic conodont biostratigraphy of the Arbuckle Mountains, southern Oklahoma: OGS Guidebook, vol. 27, 23–25.

Berger W.H., Herguera J.C., Lange C.B., Schneider R. (1994) Paleoproductivity: Flux Proxies Versus Nutrient Proxies and Other Problems Concerning the Quaternary Productivity Record. In: Zahn R., Pedersen T.F., Kaminski M.A., Labeyrie L. (eds) Carbon Cycling in the Glacial Ocean: Constraints on the Ocean's Role in Global Change. NATO ASI Series (Series I: Global Environmental Change), vol 17. Springer, Berlin, Heidelberg

Berrocoso A.J., MacLeod K.G., Martin E.E., Bourbon E., Londono C.I., Basak C. 2010. Nutrient trap for Late Cretaceous organic-rich black shales in the tropical North Atlantic. Geology, 38(12):1111-1114

Bhatia, M.R. and Crook, K.A.W. 1986. Trace element characteristics of graywackes and tectonic setting discrimination of sedimentary basins. Contributions to Mineralogy and Petrology, 92, 181–193.

Calvert S.E., Pedersen T.F. 1993. Geochemistry of Recent oxic and anoxic marine sediments: implications for the geological record. Marine Geology, 113(1-2):67-88.

Cardott, Brian J., Landis, Charles R., Curtis, Mark E., Post-oil solid bitumen network in the Woodford Shale, USA — A potential primary migration pathway, In International Journal of Coal Geology, Volume 139, 2015, Pages 106-113, ISSN 0166-5162

Comer, J.B., and Hinch, H.H., 1987, Recognizing and quantifying expulsion of oil from the Woodford Formation and age-equivalent rocks in Oklahoma and Arkansas: American Association of Petroleum Geologists Bulletin, v. 71, no. 7, p. 844–858.

Comer, J.B. 1991. Stratigraphic Analysis of the Upper Devonian Woodford Formation, Permian Basin, West Texas and Southeastern New Mexico. Texas Bureau of Economic Geology Report of Investigations, 201.

Demaison G.J., Moore G.T. 1980. Anoxic environments and oil sourcebed genesis. *AAPG Bulletin*, 64(8):1179-1209.

Ellison, S.P. 1950. Subsurface Woodford Black Shale, West Texas and Southeast New Mexico. Texas Bureau of Economic Geology Report of Investigations, 7.

Gallego-Torres D., Martínez-Ruiz F., Paytan A., Jiménez-Espejo F.J., Ortega-Huertas M. 2007. Pliocene–Holocene evolution of depositional conditions in the eastern Mediterranean: Role of anoxia vs. productivity at time of sapropel deposition. Palaeogeography, Palaeoclimatology, Palaeoecology, 246(2-4):424-439.

Goldberg, K., and Humayun, M., 2016, Geochemical paleoredox indicators in organic-rich shales of the Irati Formation, Permian of the Parana Basin, southern Brazil: Brazilian Journal of Geology, v. 46, p. 377–393.

Grinsted, A., Moore, J.C., and Jevrejeva, S., 2004, Application of the cross wavelet transform and wavelet coherence to geophysical time series: Nonlinear Processes in Geophysics, v. 11, p. 561–566.

Higley, D.K., 2014, Thermal Maturation of Petroleum Source Rocks in the Anadarko Basin Province, Colorodo, Kansas, Oklahoma, and Texas: U.S. Geological Survey Digital Data Series.

Huang J., Chu X., Jiang G., Feng L., Chang H. 2011. Hydrothermal origin of elevated iron, manganese and redox-sensitive trace elements in the c. 635 Ma Doushantuo cap carbonate. Journal of the Geological Society, 168(3):805-816.

Kübler B, and Jaboyedoff M, 2000, Illite crystallinity: Earth and Planetary Sciences, v. 331, p. 75-89

Lazar, O.R., Bochas, K.M., MacQuaker, J.H.S., Schieber, J., and Demko, T.M., 2015, Capturing Key Attributes of Fine-Grained Sedimentary Rocks in Outcrops, Cores, and Thin Section: Nomenclature and Description Guidlines : Journal of Sedimentary Research, v. 85, p. 230–246.

Miceli-Romero, A. and Philp, R.P. 2012. Organic geochemistry of the Woodford Shale, southeastern, Oklahoma: How variable can shales be? American Association of Petroleum Geologists Bulletin, 96, 493–517.

Moore, D. M., and Reynolds, R. C., 1997, X-ray Diffraction and the Identification and Analysis of Clay Minerals, v. 332, New York: Oxford university press.

Morford J.L., Emerson S., Breckel E.J., Kim S.H. 2005. Diagenesis of oxyanions (V, U, Re, and Mo) in pore waters and sediments from a continental margin. Geochimica et Cosmochimica Acta, 69(21):5021-5032.

Pearce, T.J. and Jarvis, I. 1992. Applications of geochemical data to modelling sediment dispersal patterns in distal turbidites: Late Quaternary of the Madeira abyssal plain. Journal of Sedimentary Petrology, 62, 1112–1129.

Pearce, T.J.,Besly, B.M.,Wray,D.S.andWright,D.K.1999.Chemostratigraphy:a method to improve interwell correlation in barren sequences—a case study using onshore Duckmantian/Stephanian sequences (West Midlands, UK). Sedimentary Geology, 124, 197–220.

Rowe, H., Hughes, N., and Robinson, K. (2012). The quantification and application of handheld energy-dispersive x-ray fluorescence (ED-XRF) in mudrock chemostratigraphy and geochemistry. Chemical Geology, 324, 122-131

Sageman, B.B. and Lyons, T.W. 2004. Geochemistry of fine-grained sediments and sedimentary rocks. In: Mackenzie, F. (ed.) Sediments, Diagenesis, and Sedimentary Rock. Treatise on Geochemistry, 7. Elsevier, Amsterdam, 115–158.

Shenkel, C. W., 1955. Geology of the lost springs pools area, Marion and Dickinson Counties, Kansas: Kansas Geol. Survey, Bull. 114, Pt. 6

Speakman, S.A., 2012, Introduction to PANalytical X'Pert HighScore Plus v3.0: MIT Center for Materials Science and Engineering.

Tribovillard, N., T. J. Algeo, T. Lyons, and A. Riboulleau, 2006, Trace metals as paleoredox and paleoproductivity proxies: An update: Chemical Geology, 232, 12–32

Turner, B.W., Molinares-Blanco, C.E. and Slatt, R.M. 2015. Chemostratigraphic, palynostratigraphic, and sequence-stratigraphic analysis of the Woodford Shale, Wyche Farm Quarry, Pontotoc County, Oklahoma. Interpretation, 3, SH1–SH9.

Wedepohl K.H. 1991. The composition of the upper Earth's crust and the natural cycles of selected metals. In: Merian E. (ed.) Metals and their Compounds in the Environment. VCH-Verlagsgesellschaft, Weinheim, p. 3-17

Wehner, Tyler D. 2018, Variations in mineral abundance within a single horizontal well path in the Woodford Shale, Arkoma Basin, Oklahoma. Master's Thesis, Kansas State University. 75p.

Woodrow, D., Fletcher, F., and Ahrnsbrak, W., 1973, Paleogeography and paleoclimate at the deposition sites of the Devonian Catskill and Old Red Sandstone Facies: Geological Society of America Bulletin, v. 84, p. 3051-3064.

Appendix A - HHXRF Data

Major Element Standards (HHXRF)										
	Mg Oxide %	**Al Oxide %**	**Si Oxide %**	**P Oxide %**	**S Oxide %**	**K Oxide %**	**Ca Oxide %**	**Ti Oxide %**	**Mn Oxide %**	**Fe Oxide %**
STND1	1.43506	8.23736	66.86182	0.21976	6.18403	2.91751	0.17846	0.46395	0.03087	3.57806
STND2	1.25935	8.17724	66.40763	0.19989	6.06645	2.90582	0.17722	0.46740	0.03108	3.51165
STND3	1.42397	8.24608	67.27162	0.19567	6.13341	2.95067	0.18369	0.47183	0.03145	3.56987
STND4	1.05027	8.09478	65.84190	0.21286	6.04457	2.90570	0.25140	0.46630	0.03086	3.54023
STND5	1.13953	8.21471	65.04611	0.19756	6.05720	2.86351	0.21999	0.47213	0.03074	3.66293
STND6	1.37639	8.47576	67.86286	0.20500	6.29535	2.97671	0.18786	0.46726	0.03125	3.65312
STND7	1.20605	8.39933	67.20847	0.20718	6.14061	2.90987	0.19397	0.46801	0.03096	3.57679
STND8	1.23694	8.36141	67.36520	0.21626	6.14162	2.94778	0.23748	0.45960	0.03187	3.57168
STND9	1.47156	8.60176	66.55262	0.20675	6.09006	2.98802	0.22259	0.46772	0.03079	3.66413
STND10	1.52461	8.64981	66.78178	0.21843	6.10121	2.98998	0.21403	0.47848	0.03138	3.68378
STND11	1.44510	8.27720	66.82518	0.20532	6.27908	2.93701	0.18517	0.46724	0.03146	3.67852
STND12	1.52156	9.15982	65.72006	0.18576	5.93236	3.08693	0.26361	0.47602	0.03187	3.65036
STND13	1.21324	8.26720	65.83744	0.23406	6.08196	2.86167	0.21398	0.46335	0.03052	3.61596
STND14	1.55234	8.53979	67.01077	0.21921	6.07425	2.97370	0.28161	0.45537	0.03127	3.54719
AVG Oxide %	1.34685	8.40730	66.61382	0.20884	6.11587	2.94392	0.21508	0.46748	0.03117	3.60745
Std. Dev.	0.15993	0.27266	0.76983	0.01232	0.09343	0.05857	0.03343	0.00604	0.00041	0.05751
Std. Error	0.04274	0.07287	0.20575	0.00329	0.02497	0.01565	0.00893	0.00162	0.00011	0.01537

Major Element Concentrations from Core 15-045-21557 (HHXRF)												
Box	**Depth (ft)**	**Sample Code**	**Mg Oxide %**	**Al Oxide %**	**Si Oxide %**	**P Oxide %**	**S Oxide %**	**K Oxide %**	**Ca Oxide %**	**Ti Oxide %**	**Mn Oxide %**	**Fe Oxide %**
139	1637.00	DCCM-1637	2.68798	2.89116	11.88041	0.00000	1.04033	0.74310	45.18053	0.11494	0.02370	1.18205
139	1637.33	DCCM-1637-4	1.30329	1.83422	8.38533	0.00000	2.37604	0.42137	40.75165	0.06924	0.02077	1.75334
139	1637.67	DCCM-1637-8	1.45568	1.39696	7.67523	0.00000	1.14489	0.42499	47.39344	0.07183	0.02290	1.10007
139	1638.00	DCCM-1638	2.10295	2.40972	11.03774	0.00000	0.56281	0.76352	43.82728	0.11643	0.02611	1.07425
139	1638.33	DCCM-1638-4	0.41673	0.83841	7.36679	0.00000	0.47138	0.46494	31.32851	0.06088	0.02585	0.97109
139	1638.67	DCCM-1638-8	10.81164	4.44917	19.77008	0.01577	0.81062	1.08804	34.65039	0.19152	0.03536	1.81071
139	1639.00	DCCM-1639	1.87894	13.42693	56.15412	0.20720	1.64880	5.49406	3.48663	0.68099	0.03071	2.93333
139	1639.33	DCCM-1639-4	1.49732	14.21183	56.00235	0.04419	1.03126	5.42456	1.63458	0.67844	0.02986	2.73711
139	1639.67	DCCM-1639-8	-0.15490	8.33975	38.16249	0.03586	0.82955	3.26071	0.17077	0.50246	0.02451	2.46229
139	1640.00	DCCM-1640	1.47493	14.21226	64.15087	0.04785	0.75033	5.43853	0.53796	0.74925	0.03190	2.63966
140	1640.33	DCCM-1640-4	1.50272	12.93662	62.97595	0.07751	3.33692	5.13489	0.53670	0.72661	0.03176	2.92085
140	1640.67	DCCM-1640-8	1.33053	11.92060	63.72081	0.05715	0.90287	4.81170	1.63352	0.71379	0.03336	2.17036
140	1641.00	DCCM-1641	1.92604	12.78077	59.53375	0.07148	2.85308	4.85713	1.65679	0.66116	0.02962	3.79074
140	1641.33	DCCM-1641-4	1.69420	14.80430	58.18479	0.05255	2.83890	5.56166	0.81919	0.70523	0.02906	3.48101
140	1641.67	DCCM-1641-8	1.56130	14.53712	55.86891	0.04731	2.21575	5.47403	1.19406	0.64532	0.02712	3.70633
140	1642.00	DCCM-1642	0.99595	13.46156	50.01772	0.02352	1.91425	5.39308	1.67853	0.62716	0.02823	3.48677
140	1642.33	DCCM-1642-4	1.12986	12.08277	60.32713	0.04104	1.16169	4.94924	1.03932	0.70273	0.03151	2.71044
140	1642.67	DCCM-1642-8	2.06694	14.04143	54.60841	0.04245	0.98376	5.22972	4.18039	0.71870	0.03335	3.00995
140	1643.00	DCCM-1643	0.78380	16.17902	53.19496	0.00913	0.59330	5.39033	0.30616	0.61629	0.02866	3.73367
140	1643.33	DCCM-1643-4	1.46646	12.12329	48.75501	0.03144	1.04754	4.86054	4.97449	0.70799	0.03222	3.15707
140	1643.67	DCCM-1643-8	3.07567	12.90758	48.64321	0.06575	1.08287	4.50916	9.86906	0.65590	0.03693	3.23804
140	1644.00	DCCM-1644	4.60980	11.20316	41.39624	0.04467	1.27250	3.77499	13.67177	0.50808	0.03941	3.70641
140	1644.33	DCCM-1644-4	4.73494	11.42059	42.96741	0.07251	0.84256	3.71556	13.42965	0.54449	0.04113	3.57521
140	1644.67	DCCM-1644-8	3.86453	12.31350	46.03723	0.07839	1.43914	4.11823	10.17960	0.57881	0.03794	3.89721
140	1645.00	DCCM-1645	2.93729	13.64286	50.51886	0.06997	2.22500	4.69049	6.77968	0.64414	0.03307	3.93016
140	1645.33	DCCM-1645-4	7.74095	6.69680	37.04881	0.14431	0.78660	2.13128	20.13384	0.41039	0.06515	3.49088
140	1645.67	DCCM-1645-8	1.83009	15.75299	57.88873	0.04143	1.05448	5.57565	2.31703	0.70574	0.03146	3.16504
140	1646.00	DCCM-1646	1.79473	14.80045	56.61733	0.03520	0.86359	5.49693	2.87652	0.71513	0.03197	3.09420
140	1646.33	DCCM-1646-4	1.03693	15.14508	48.12388	0.02924	2.79954	5.18632	0.28388	0.60381	0.02696	5.07302
140	1646.67	DCCM-1646-8	0.17363	14.27146	45.18403	0.00000	1.90069	4.26321	0.16482	0.42764	0.02271	3.95217
140	1647.00	DCCM-1647	1.43912	16.72563	51.99237	0.02945	2.20911	5.24034	0.23936	0.57904	0.03056	4.88029
140	1647.33	DCCM-1647-4	1.38045	16.13789	50.58495	0.02913	2.25411	5.23495	0.22540	0.58699	0.03166	4.98855
140	1647.67	DCCM-1647-8	4.66327	15.03767	43.49508	0.32687	20.10766	4.26432	0.21275	0.50535	0.01939	10.24497
140	1648.00	DCCM-1648	1.28688	16.00024	50.17179	0.02517	2.37518	5.22104	0.32448	0.57664	0.03192	4.90422
140	1648.33	DCCM-1648-4	0.79936	15.03354	46.71690	0.01486	1.85890	4.74585	0.22444	0.55354	0.02993	4.78577
140	1648.67	DCCM-1648-8	0.99895	15.25793	46.67967	0.01002	1.86044	4.98544	0.21875	0.58699	0.03090	4.84663

Major Element Concentrations from Core 15-045-21557 (HHXRF)												
Box	**Depth (ft)**	**Sample Code**	**Mg Oxide %**	**Al Oxide %**	**Si Oxide %**	**P Oxide %**	**S Oxide %**	**K Oxide %**	**Ca Oxide %**	**Ti Oxide %**	**Mn Oxide %**	**Fe Oxide %**
140	1649.00	DCCM-1649	1.13836	16.32397	49.28507	0.02144	1.99273	5.19089	0.24929	0.58823	0.03095	5.01566
140	1649.33	DCCM-1649-4	1.14886	15.61654	48.45826	0.01421	1.25782	5.19943	0.48096	0.60255	0.03177	4.88369
140	1649.67	DCCM-1649-8	1.41196	16.43992	50.58972	0.01869	1.35573	5.31597	0.51962	0.58173	0.03119	5.00866
140	1650.00	DCCM-1650	0.93127	15.88983	49.35670	0.01371	1.36244	5.23657	0.41745	0.57282	0.03126	5.02584
140	1650.33	DCCM-1650-4	1.34868	16.20823	49.19904	0.01538	1.38843	5.23139	0.55879	0.58727	0.03232	4.99180
140	1650.67	DCCM-1650-8	1.57804	17.04661	52.13219	0.02352	1.23342	5.42189	0.66283	0.63181	0.03351	4.94694
140	1651.00	DCCM-1651	1.54594	16.13477	49.57907	0.01834	1.76878	5.25991	0.59639	0.60279	0.03122	5.18550
140	1651.33	DCCM-1651-4	1.46884	16.70789	51.01190	0.01738	1.12012	5.37478	0.64632	0.61415	0.03256	4.95599
140	1651.67	DCCM-1651-8	1.44213	16.81076	50.56411	0.03524	2.21267	5.37408	0.62639	0.59711	0.03160	5.21328
141	1652.00	DCCM-1652	1.74948	17.07574	51.47462	0.02661	1.41331	5.38945	0.87671	0.63224	0.03408	5.04657
141	1652.33	DCCM-1652-4	1.83453	16.35980	50.32935	0.02214	1.83642	5.22540	0.83217	0.64140	0.03289	5.20471
141	1652.67	DCCM-1652-8	1.25670	15.57591	49.16234	0.02405	1.63279	5.08365	0.86803	0.62772	0.03228	5.06094
141	1653.00	DCCM-1653	1.14459	15.37767	47.04241	0.01079	1.82413	5.04043	0.87388	0.64491	0.03122	5.23813
141	1653.33	DCCM-1653-4	1.51793	16.03379	48.73795	0.02271	1.75741	5.09430	0.93030	0.60624	0.03169	5.26900
141	1653.67	DCCM-1653-8	1.49699	16.18945	47.50631	0.01804	1.80708	5.13311	0.91929	0.65936	0.03146	5.32606
141	1654.00	DCCM-1654	1.64616	16.22003	48.60020	0.02195	1.88390	5.04912	1.35593	0.60350	0.03347	5.28577
141	1654.33	DCCM-1654-4	1.42701	15.72841	45.91578	0.01648	1.54262	5.02135	1.94584	0.56898	0.03588	5.31594
141	1654.67	DCCM-1654-8	1.53396	15.97131	48.08535	0.02001	1.72722	4.97492	1.70324	0.55447	0.03309	5.24119
141	1655.00	DCCM-1655	1.45927	15.93334	47.96656	0.01917	1.61134	5.12253	1.30580	0.58243	0.03353	5.30437
141	1655.33	DCCM-1655-4	1.17315	15.07355	45.46625	0.01163	1.76210	5.01294	1.23721	0.57980	0.03262	5.38747
141	1655.67	DCCM-1655-8	1.13237	15.32887	46.87873	0.01102	1.56482	5.06966	1.09861	0.55845	0.03145	5.28473
141	1656.00	DCCM-1656	1.35894	15.95033	49.35873	0.01687	1.74220	5.03739	1.13672	0.58196	0.03246	5.33879
141	1656.33	DCCM-1656-4	1.18657	15.46928	48.59426	0.01827	1.52800	4.67735	2.11721	0.54284	0.02971	4.94251
141	1656.67	DCCM-1656-8	1.48166	15.69130	49.15971	0.02298	1.75848	5.02548	1.84189	0.60826	0.03320	5.15715
141	1657.00	DCCM-1657	0.66764	14.51495	46.12076	0.00590	1.84101	4.48355	1.22013	0.53439	0.02872	4.84926
141	1657.33	DCCM-1657-4	1.30389	15.45538	48.59669	0.01394	1.79892	4.82059	1.20450	0.58802	0.03068	5.05502
141	1657.67	DCCM-1657-8	1.47989	16.09073	49.00825	0.02695	1.63598	5.11132	1.36405	0.61253	0.03250	5.23137
141	1658.00	DCCM-1658	1.43710	15.95482	48.18428	0.01752	1.86083	5.01899	1.16502	0.58840	0.03077	5.26854
141	1658.33	DCCM-1658-4	1.37916	16.11448	49.31882	0.02160	2.01112	5.03098	1.15272	0.60345	0.03219	5.32199
141	1658.67	DCCM-1658-8	1.46064	15.63978	48.66524	0.02018	1.65996	5.03701	1.36253	0.61474	0.03132	5.18904
141	1659.00	DCCM-1659	1.53828	15.73058	49.10091	0.02992	1.90351	4.94294	1.51264	0.60026	0.03220	5.20930
141	1659.33	DCCM-1659-4	1.78335	15.70306	50.24806	0.03681	2.63930	4.86284	1.98639	0.62562	0.03182	5.13229
141	1659.67	DCCM-1659-8	1.62267	15.15372	47.90560	0.03268	2.30835	4.88778	1.94734	0.62111	0.03300	5.26647
141	1660.00	DCCM-1660	1.55761	15.83712	48.95042	0.02812	1.97327	5.05754	1.61936	0.62741	0.03346	5.27319
141	1660.33	DCCM-1660-4	1.02796	15.02680	46.47071	0.01002	1.49799	4.85526	1.33654	0.57602	0.03148	5.04481
141	1660.67	DCCM-1660-8	1.47022	15.70932	48.99344	0.01782	1.47715	4.99674	1.88696	0.61123	0.03366	5.12766

Major Element Concentrations from Core 15-045-21557 (HHXRF)												
Box	**Depth (ft)**	**Sample Code**	**Mg Oxide %**	**Al Oxide %**	**Si Oxide %**	**P Oxide %**	**S Oxide %**	**K Oxide %**	**Ca Oxide %**	**Ti Oxide %**	**Mn Oxide %**	**Fe Oxide %**
141	1661.00	DCCM-1661	1.60843	15.52088	48.55816	0.03696	2.91062	5.05804	1.75543	0.61990	0.03198	5.62405
141	1661.33	DCCM-1661-4	1.30309	15.79532	49.42998	0.01970	1.65436	5.08925	0.95663	0.60693	0.03202	5.17875
141	1661.67	DCCM-1661-8	1.14541	15.47179	48.87224	0.01563	1.45973	5.09152	1.24827	0.60034	0.03181	5.08495
141	1662.00	DCCM-1662	1.42242	15.38874	48.62454	0.01908	1.70604	4.98373	1.29052	0.62952	0.03089	5.14568
141	1662.33	DCCM-1662-4	1.30223	16.15377	48.70227	0.01684	1.70163	5.09726	1.01113	0.62996	0.03091	5.10114
141	1662.67	DCCM-1662-8	0.14927	11.39241	35.72510	0.00000	1.87442	4.22987	0.93618	0.55113	0.02653	4.91609
141	1663.00	DCCM-1663	1.56302	16.09926	49.46812	0.02605	2.11896	5.09212	1.06519	0.61722	0.03143	5.25955
141	1663.33	DCCM-1663-4	1.75714	15.73123	47.53784	0.03978	3.51065	4.91933	1.16868	0.57881	0.02926	6.07483
142	1663.67	DCCM-1663-8	1.34522	15.84038	48.30734	0.02340	2.13530	5.01848	1.07339	0.58340	0.03154	5.36474
142	1664.00	DCCM-1664	-0.06725	7.82721	27.06999	0.00000	1.47852	3.62650	0.81317	0.51134	0.02505	4.65574
142	1664.33	DCCM-1664-4	1.18135	16.12358	48.20992	0.01135	1.44212	5.21574	1.03883	0.59644	0.03097	5.05490
142	1664.67	DCCM-1664-8	4.09194	15.51447	47.82789	0.23525	12.79192	4.73011	3.06538	0.66743	0.02470	7.35114
142	1665.00	DCCM-1665	1.60578	15.74323	52.44365	0.02971	1.81796	5.17424	1.33734	0.70992	0.03120	4.76784
142	1665.33	DCCM-1665-4	1.55979	15.63729	50.59088	0.02399	1.76813	5.11629	1.18325	0.70901	0.03117	4.71617
142	1665.67	DCCM-1665-8	1.59821	16.02516	50.46736	0.02781	2.51029	5.23856	1.00598	0.65676	0.03045	4.99532
142	1666.00	DCCM-1666	1.62728	16.03128	49.72166	0.04464	3.39366	5.24059	0.93091	0.63374	0.02886	5.44692
142	1666.33	DCCM-1666-4	1.70883	15.44087	47.88801	0.05209	3.53823	5.04903	1.59735	0.59752	0.02890	5.59167
142	1666.67	DCCM-1666-8	1.36842	15.95153	49.07138	0.03671	2.83328	5.19764	1.09728	0.61015	0.02912	5.28753
142	1667.00	DCCM-1667	2.29071	15.23536	49.73808	0.08204	5.94826	5.03759	1.48558	0.65038	0.02992	5.54573
142	1667.33	DCCM-1667-4	1.27688	14.78696	52.47620	0.08038	0.76291	5.06582	2.17316	0.70543	0.03345	3.97545
142	1667.67	DCCM-1667-8	1.68415	15.94315	55.10017	0.03141	0.84259	5.34413	1.40248	0.70055	0.03359	4.11558
142	1668.00	DCCM-1668	1.89855	15.92221	53.33808	0.03858	1.69482	5.17261	1.61400	0.68368	0.02917	4.79597
142	1668.33	DCCM-1668-4	1.45552	15.78081	51.26265	0.02439	1.35074	5.24267	1.41456	0.66646	0.03028	4.23751
142	1668.67	DCCM-1668-8	1.55691	15.37427	48.66285	0.03700	2.73396	5.06995	2.01119	0.62280	0.02914	4.94023
142	1669.00	DCCM-1669	1.92570	14.78285	47.24020	0.04066	2.72451	4.91682	3.35004	0.64357	0.02992	4.72767
142	1669.33	DCCM-1669-4	2.26389	14.51155	49.11353	0.03350	1.28084	4.91269	5.03619	0.67407	0.03311	4.06726
142	1669.67	DCCM-1669-8	3.89541	11.72228	41.80361	0.05140	1.38698	3.89898	11.45627	0.58044	0.03861	3.96958
142	1670.00	DCCM-1670	3.43171	10.61224	38.42748	0.03039	0.94024	3.54342	12.90004	0.54521	0.04527	3.59537
142	1670.33	DCCM-1670-4	2.77822	13.22781	49.03091	0.04341	1.13313	4.48530	6.80997	0.67531	0.03862	3.68313
142	1670.67	DCCM-1670-8	0.95370	13.36360	48.38910	0.02118	1.12679	4.77096	2.17953	0.70273	0.03182	3.72982
142	1671.00	DCCM-1671	1.83643	16.02704	51.60641	0.03329	1.77390	5.30777	1.62107	0.65823	0.03068	4.45231
142	1671.33	DCCM-1671-4	0.98018	14.59628	45.78834	0.01759	2.10107	4.93734	1.64373	0.61305	0.02895	4.50286
142	1671.67	DCCM-1671-8	2.47319	15.35372	52.40608	0.08089	4.66911	4.99756	2.30621	0.67421	0.03126	5.27435
142	1672.00	DCCM-1672	1.46223	15.57510	53.95116	0.03482	1.41170	5.17823	1.53393	0.70468	0.03116	4.06704
142	1672.33	DCCM-1672-4	1.61996	15.73305	50.44315	0.04887	3.85741	5.08325	1.01898	0.64645	0.02945	5.36898
142	1672.67	DCCM-1672-8	1.34515	15.67409	49.08199	0.03859	2.98820	5.05191	1.55208	0.63421	0.02912	4.88731

Major Element Concentrations from Core 15-045-21557 (HHXRF)												
Box	**Depth (ft)**	**Sample Code**	**Mg Oxide %**	**Al Oxide %**	**Si Oxide %**	**P Oxide %**	**S Oxide %**	**K Oxide %**	**Ca Oxide %**	**Ti Oxide %**	**Mn Oxide %**	**Fe Oxide %**
142	1673.00	DCCM-1673	1.68910	15.40292	48.63116	0.05046	3.41786	4.98913	1.53769	0.61168	0.02832	5.04940
142	1673.33	DCCM-1673-4	1.87478	14.85360	48.34791	0.07414	4.72209	4.80352	1.86935	0.61059	0.02778	5.47014
142	1673.67	DCCM-1673-8	0.68289	12.31389	39.12701	0.02182	3.18244	4.49185	1.82987	0.58114	0.02713	4.95643
142	1674.00	DCCM-1674	1.68802	15.82630	49.71667	0.05265	3.25339	5.05446	1.65689	0.60839	0.02920	4.86471
142	1674.33	DCCM-1674-4	1.34889	16.07856	52.61589	0.02958	1.24488	5.29763	1.58066	0.67621	0.03131	3.88605
142	1674.67	DCCM-1674-8	1.21813	15.64505	48.22241	0.03885	3.00648	5.04862	1.36415	0.60497	0.02779	4.82447
143	1675.00	DCCM-1675	1.54912	15.50452	49.47416	0.03820	2.92957	5.11798	1.64646	0.61795	0.02932	4.71559
143	1675.33	DCCM-1675-4	1.93080	15.07082	49.45909	0.06424	3.84346	4.87708	2.53100	0.61561	0.02895	4.87908
143	1675.67	DCCM-1675-8	1.12928	16.79918	53.06582	0.01899	1.06171	5.52776	0.68710	0.60487	0.02943	4.14744
143	1676.00	DCCM-1676	1.43231	15.76772	48.24362	0.05121	4.62866	5.12093	0.55165	0.54236	0.02720	5.45049
143	1676.33	DCCM-1676-4	1.47236	15.99344	49.08738	0.06585	5.99094	5.14113	0.84985	0.62733	0.02935	4.98144
143	1676.67	DCCM-1676-8	0.96527	16.68204	52.81804	0.01956	1.02144	5.55222	0.39359	0.65274	0.03034	3.97264
143	1677.00	DCCM-1677	1.80122	14.89024	44.09725	0.10457	7.66967	4.80846	1.43628	0.55517	0.02654	5.80917
143	1677.33	DCCM-1677-4	1.59996	15.88651	48.23158	0.05844	4.75553	5.20697	1.97348	0.56208	0.02719	5.09185
143	1677.67	DCCM-1677-8	2.64812	8.15328	51.60994	0.19601	0.84491	2.48491	11.15095	0.33450	0.03816	1.71792
143	1678.00	DCCM-1678	14.03771	3.79407	12.30081	0.00000	0.84653	0.78855	35.01069	0.11851	0.03869	2.83996
143	1678.33	DCCM-1678-4	10.81910	2.67020	11.17213	0.00000	0.81837	0.63386	33.35138	0.10278	0.03838	3.01630
143	1678.67	DCCM-1678-8	15.14197	2.03877	9.65499	0.00000	1.31922	0.47972	34.85016	0.08891	0.03774	3.14633
143	1679.00	DCCM-1679	18.01914	2.43946	10.65768	0.00000	0.86938	0.51953	36.92489	0.09624	0.03955	2.86855
143	1679.33	DCCM-1679-4	13.97204	3.38171	12.08265	0.00000	0.86258	0.61167	34.37323	0.09200	0.03691	2.95782
143	1679.67	DCCM-1679-8	14.91771	2.98177	11.64168	0.00000	1.00839	0.63845	34.02038	0.10264	0.03702	2.53902
143	1680.00	DCCM-1680	11.70645	2.15426	9.47006	0.00000	0.73403	0.48734	33.05895	0.09127	0.03490	2.17776
143	1680.33	DCCM-1680-4	17.26614	2.25497	9.33630	0.00000	1.25278	0.45993	36.63938	0.09225	0.03515	2.83885
143	1680.67	DCCM-1680-8	18.48269	1.75271	7.94150	0.00000	0.90981	0.37400	36.51454	0.07155	0.03256	2.35442
143	1681.00	DCCM-1681	12.88831	2.45656	10.45681	0.00000	1.04174	0.64517	34.34201	0.09892	0.03394	1.81686
143	1681.33	DCCM-1681-4	2.10415	3.14479	16.92319	0.00000	1.23311	0.67793	47.00461	0.10492	0.02080	1.15505
143	1681.67	DCCM-1681-8	1.41705	0.57429	4.50015	0.00000	0.43976	0.14546	55.70148	0.02613	0.02015	0.85033
143	1682.00	DCCM-1682	1.21793	0.38498	4.45480	0.00000	0.47213	0.16341	51.59485	0.02601	0.02025	0.84662
143	1682.33	DCCM-1682-4	0.47965	0.00000	3.77196	0.00000	0.36574	0.10026	40.17517	0.01468	0.01992	0.84250
143	1682.67	DCCM-1682-8	1.49574	0.57754	4.62549	0.00000	0.55200	0.17077	54.05495	0.03322	0.02007	0.88477
143	1683.00	DCCM-1683	1.65898	0.68795	3.87518	0.00000	0.58908	0.16003	57.45804	0.03552	0.02018	0.80924

Minor/Trace Element Standards (HHXRF)						
	Ba Oxide %	**Ni Oxide %**	**Cu Oxide %**	**Zr Oxide %**	**Mo Oxide %**	**Zn Oxide %**
STND1	0.27152	0.01792	0.01395	0.01477	0.01003	0.06653
STND2	0.18052	0.01716	0.01395	0.01519	0.01073	0.06266
STND3	0.09334	0.01733	0.01377	0.01488	0.01050	0.06306
STND4	0.19641	0.01756	0.01473	0.01508	0.01109	0.06640
STND5	0.10352	0.01745	0.01415	0.01547	0.01036	0.06235
STND6	0.20609	0.01703	0.01373	0.01514	0.01075	0.06255
STND7	0.23463	0.01800	0.01398	0.01534	0.01161	0.06402
STND8	0.08802	0.01815	0.01373	0.01534	0.01058	0.06579
STND9	0.24573	0.01746	0.01322	0.01539	0.01098	0.06237
STND10	0.21716	0.01813	0.01389	0.01520	0.01038	0.06497
STND11	0.18045	0.01845	0.01437	0.01531	0.01046	0.06333
STND12	0.16586	0.01684	0.01380	0.01443	0.01095	0.06311
AVG Oxide %	0.18194	0.01762	0.01394	0.01513	0.01070	0.06393
Std. Dev.	0.06029	0.00050	0.00037	0.00030	0.00042	0.00159
Std. Error	0.01740	0.00014	0.00011	0.00009	0.00012	0.00046

Minor/Trace Element Concentrations from Core 15-045-21557 (HHXRF)								
Box	**Depth**	**Sample Code**	**Ba Oxide %**	**Ni Oxide %**	**Cu Oxide %**	**Zr Oxide %**	**Mo Oxide %**	**Zn Oxide %**
139	1637	DCCM-1637	0.01959	0.00046	0.00089	0.00572	0.00000	0.00072
139	1637.3333	DCCM-1637-4	0.00000	0.00188	0.00102	0.00442	0.00000	0.00069
139	1637.6667	DCCM-1637-8	0.00000	0.00155	0.00067	0.00472	0.00000	0.00055
139	1638	DCCM-1638	0.00000	0.00116	0.00090	0.00722	0.00000	0.00065
139	1638.3333	DCCM-1638-4	0.00000	0.00022	0.00082	0.00697	0.00000	0.00083
139	1638.6667	DCCM-1638-8	0.00000	0.00134	0.00015	0.00839	0.00000	0.00040
139	1639	DCCM-1639	0.02661	0.00909	0.00164	0.02326	0.00082	0.00281
139	1639.3333	DCCM-1639-4	0.00161	0.00979	0.00158	0.02509	0.00056	0.00348
139	1639.6667	DCCM-1639-8	0.01607	0.00837	0.00141	0.03089	0.00175	0.00493
139	1640	DCCM-1640	0.11777	0.00690	0.00118	0.02820	0.00082	0.00446
140	1640.3333	DCCM-1640-4	0.20583	0.01114	0.00179	0.02743	0.00126	0.01059
140	1640.6667	DCCM-1640-8	0.08125	0.00461	0.00116	0.03822	0.00351	0.00603
140	1641	DCCM-1641	0.00000	0.01755	0.00325	0.02778	0.00180	0.01320
140	1641.3333	DCCM-1641-4	0.15029	0.01108	0.00225	0.02546	0.00111	0.00763
140	1641.6667	DCCM-1641-8	0.10293	0.01413	0.00233	0.02289	0.00147	0.00444
140	1642	DCCM-1642	0.12221	0.02146	0.00319	0.02264	0.00094	0.00513
140	1642.3333	DCCM-1642-4	0.09920	0.00708	0.00158	0.03481	0.00268	0.00849
140	1642.6667	DCCM-1642-8	0.09593	0.00901	0.00157	0.02743	0.00162	0.00436
140	1643	DCCM-1643	0.06141	0.00738	0.00234	0.01990	0.00005	0.00665
140	1643.3333	DCCM-1643-4	0.09550	0.00786	0.00142	0.02680	0.00072	0.00439
140	1643.6667	DCCM-1643-8	0.06923	0.00660	0.00139	0.02302	0.00047	0.00609
140	1644	DCCM-1644	0.11894	0.00500	0.00081	0.01581	0.00008	0.00510
140	1644.3333	DCCM-1644-4	0.07623	0.00478	0.00134	0.01744	0.00036	0.00497
140	1644.6667	DCCM-1644-8	0.06089	0.00719	0.00147	0.01810	0.00051	0.00477
140	1645	DCCM-1645	0.04022	0.00800	0.00237	0.02441	0.00128	0.00897
140	1645.3333	DCCM-1645-4	0.04353	0.00410	0.00197	0.02047	0.00081	0.01730

140	1645.6667	DCCM-1645-8	0.07867	0.01040	0.00190	0.02669	0.00130	0.00438
140	1646	DCCM-1646	0.09354	0.01017	0.00217	0.02722	0.00099	0.00453
140	1646.3333	DCCM-1646-4	0.01478	0.00830	0.00303	0.01869	0.00004	0.00491
140	1646.6667	DCCM-1646-8	0.10560	0.00707	0.00318	0.01803	0.00066	0.00594
140	1647	DCCM-1647	0.02157	0.01082	0.00301	0.01835	0.00072	0.01087
140	1647.3333	DCCM-1647-4	0.16489	0.01143	0.00291	0.01775	0.00142	0.01131
140	1647.6667	DCCM-1647-8	0.00000	0.01054	0.01685	0.01362	0.00000	0.13752
140	1648	DCCM-1648	0.09133	0.01117	0.00325	0.01825	0.00155	0.01649
140	1648.3333	DCCM-1648-4	0.00000	0.01152	0.00386	0.01826	0.00094	0.01599
140	1648.6667	DCCM-1648-8	0.00000	0.01046	0.00357	0.01868	0.00182	0.01511
140	1649	DCCM-1649	0.10116	0.00963	0.00340	0.01833	0.00190	0.01508
140	1649.3333	DCCM-1649-4	0.13239	0.00980	0.00336	0.01914	0.00094	0.01634
140	1649.6667	DCCM-1649-8	0.20626	0.01019	0.00335	0.01861	0.00109	0.01859
140	1650	DCCM-1650	0.22291	0.00991	0.00298	0.01840	0.00112	0.01433
140	1650.3333	DCCM-1650-4	0.26595	0.00952	0.00305	0.01837	0.00095	0.01500
140	1650.6667	DCCM-1650-8	0.15476	0.01002	0.00362	0.01960	0.00017	0.01652
140	1651	DCCM-1651	0.20245	0.01031	0.00368	0.01917	0.00022	0.01624
140	1651.3333	DCCM-1651-4	0.09245	0.00889	0.00347	0.01923	0.00029	0.01461
140	1651.6667	DCCM-1651-8	0.04503	0.00882	0.00299	0.01835	0.00003	0.01616
141	1652	DCCM-1652	0.19095	0.00932	0.00370	0.01953	0.00069	0.01957
141	1652.3333	DCCM-1652-4	0.15779	0.01084	0.00344	0.01978	0.00131	0.01351
141	1652.6667	DCCM-1652-8	0.16170	0.00963	0.00309	0.01983	0.00133	0.01011
141	1653	DCCM-1653	0.15944	0.01017	0.00303	0.01998	0.00123	0.00706
141	1653.3333	DCCM-1653-4	0.08775	0.01063	0.00296	0.01953	0.00031	0.00726
141	1653.6667	DCCM-1653-8	0.09177	0.01109	0.00359	0.01989	0.00024	0.00995
141	1654	DCCM-1654	0.06725	0.00974	0.00322	0.01890	0.00122	0.01163
141	1654.3333	DCCM-1654-4	0.15552	0.00911	0.00307	0.01726	0.00140	0.01022
141	1654.6667	DCCM-1654-8	0.01562	0.00975	0.00353	0.01773	0.00080	0.01366

141	1655	DCCM-1655	0.17248	0.00986	0.00313	0.01765	0.00099	0.01480
141	1655.3333	DCCM-1655-4	0.11462	0.00947	0.00331	0.01811	0.00173	0.01307
141	1655.6667	DCCM-1655-8	0.08077	0.00929	0.00316	0.01771	0.00114	0.00974
141	1656	DCCM-1656	0.14259	0.01022	0.00300	0.01925	0.00070	0.01183
141	1656.3333	DCCM-1656-4	0.06648	0.00962	0.00331	0.01910	0.00147	0.00995
141	1656.6667	DCCM-1656-8	0.01203	0.01034	0.00336	0.01913	0.00071	0.00959
141	1657	DCCM-1657	0.21540	0.01066	0.00410	0.02063	0.00174	0.01028
141	1657.3333	DCCM-1657-4	0.17520	0.01037	0.00339	0.01999	0.00161	0.00951
141	1657.6667	DCCM-1657-8	0.16877	0.00977	0.00306	0.01964	0.00127	0.00960
141	1658	DCCM-1658	0.12674	0.00997	0.00284	0.01867	0.00104	0.00685
141	1658.3333	DCCM-1658-4	0.06222	0.00980	0.00293	0.01934	0.00034	0.00706
141	1658.6667	DCCM-1658-8	0.16210	0.00959	0.00469	0.01927	0.00043	0.03591
141	1659	DCCM-1659	0.07291	0.00991	0.00328	0.01985	0.00091	0.00731
141	1659.3333	DCCM-1659-4	0.21283	0.01005	0.00309	0.02044	0.00236	0.00713
141	1659.6667	DCCM-1659-8	0.04453	0.00919	0.00275	0.01935	0.00163	0.00639
141	1660	DCCM-1660	0.19460	0.00923	0.00275	0.02003	0.00134	0.00741
141	1660.3333	DCCM-1660-4	0.15364	0.00899	0.00267	0.01840	0.00144	0.00776
141	1660.6667	DCCM-1660-8	0.15827	0.00906	0.00267	0.01828	0.00111	0.00679
141	1661	DCCM-1661	0.06395	0.00893	0.00261	0.01872	0.00000	0.00657
141	1661.3333	DCCM-1661-4	0.07728	0.00947	0.00290	0.01889	0.00000	0.00735
141	1661.6667	DCCM-1661-8	0.08355	0.00900	0.00284	0.01890	0.00014	0.00866
141	1662	DCCM-1662	0.18746	0.00920	0.00313	0.01971	0.00042	0.00883
141	1662.3333	DCCM-1662-4	0.14432	0.00934	0.00305	0.01961	0.00072	0.00773
141	1662.6667	DCCM-1662-8	0.13778	0.00872	0.00315	0.01716	0.00071	0.01256
141	1663	DCCM-1663	0.15149	0.01007	0.00330	0.01939	0.00144	0.00662
141	1663.3333	DCCM-1663-4	0.16461	0.01090	0.00336	0.01820	0.00225	0.00691
142	1663.6667	DCCM-1663-8	0.11774	0.00992	0.00346	0.01915	0.00246	0.00739
142	1664	DCCM-1664	0.16767	0.00875	0.00293	0.01723	0.00065	0.00652

142	1664.3333	DCCM-1664-4	0.17038	0.00876	0.00260	0.01889	0.00000	0.00679
142	1664.6667	DCCM-1664-8	0.13054	0.00965	0.00359	0.02221	0.00165	0.00725
142	1665	DCCM-1665	0.11736	0.00838	0.00296	0.02221	0.00048	0.00849
142	1665.3333	DCCM-1665-4	0.02960	0.00835	0.00256	0.02293	0.00047	0.00824
142	1665.6667	DCCM-1665-8	0.21565	0.00973	0.00405	0.02143	0.00011	0.01729
142	1666	DCCM-1666	0.16243	0.01042	0.00380	0.02011	0.00066	0.01027
142	1666.3333	DCCM-1666-4	0.16213	0.01160	0.00425	0.02005	0.00179	0.00688
142	1666.6667	DCCM-1666-8	0.10862	0.01037	0.00409	0.02083	0.00079	0.00790
142	1667	DCCM-1667	0.09587	0.00898	0.00287	0.02337	0.00095	0.00884
142	1667.3333	DCCM-1667-4	0.18916	0.00579	0.00175	0.02459	0.00078	0.00805
142	1667.6667	DCCM-1667-8	0.08521	0.00663	0.00239	0.02243	0.00077	0.00748
142	1668	DCCM-1668	0.07403	0.00902	0.00518	0.02204	0.00000	0.03157
142	1668.3333	DCCM-1668-4	0.07786	0.00791	0.00256	0.02220	0.00000	0.00647
142	1668.6667	DCCM-1668-8	0.18083	0.01029	0.00371	0.02198	0.00188	0.00636
142	1669	DCCM-1669	0.18050	0.00928	0.00330	0.02130	0.00094	0.00582
142	1669.3333	DCCM-1669-4	0.13984	0.00711	0.00228	0.02186	0.00000	0.00553
142	1669.6667	DCCM-1669-8	0.15970	0.00637	0.00181	0.02140	0.00088	0.00428
142	1670	DCCM-1670	0.00000	0.00486	0.00127	0.02047	0.00069	0.00393
142	1670.3333	DCCM-1670-4	0.08313	0.00579	0.00154	0.02403	0.00083	0.00512
142	1670.6667	DCCM-1670-8	0.16781	0.00602	0.00175	0.02395	0.00114	0.00541
142	1671	DCCM-1671	0.05421	0.00805	0.00274	0.02156	0.00000	0.00562
142	1671.3333	DCCM-1671-4	0.07224	0.00907	0.00376	0.02089	0.00017	0.01311
142	1671.6667	DCCM-1671-8	0.12545	0.00900	0.00477	0.02243	0.00045	0.00604
142	1672	DCCM-1672	0.02435	0.00640	0.00183	0.02356	0.00059	0.00511
142	1672.3333	DCCM-1672-4	0.08622	0.01023	0.00431	0.02217	-0.00022	0.00685
142	1672.6667	DCCM-1672-8	0.13646	0.01060	0.00451	0.02237	0.00122	0.00576
142	1673	DCCM-1673	0.12340	0.01008	0.00429	0.02069	0.00124	0.00583
142	1673.3333	DCCM-1673-4	0.02075	0.01185	0.00477	0.02192	0.00302	0.00531

142	1673.6667	DCCM-1673-8	0.24149	0.00973	0.00421	0.01995	0.00183	0.00531
142	1674	DCCM-1674	0.17603	0.00998	0.00438	0.02089	0.00134	0.00571
142	1674.3333	DCCM-1674-4	0.02730	0.00812	0.00257	0.02218	0.00090	0.00532
142	1674.6667	DCCM-1674-8	0.05255	0.01013	0.00464	0.02138	0.00101	0.00548
143	1675	DCCM-1675	0.12403	0.00945	0.00459	0.02082	0.00066	0.00499
143	1675.3333	DCCM-1675-4	0.16432	0.01199	0.00469	0.02167	0.00226	0.00534
143	1675.6667	DCCM-1675-8	0.26308	0.00686	0.00172	0.01884	0.00041	0.00418
143	1676	DCCM-1676	0.20139	0.01126	0.00534	0.01792	0.00359	0.00458
143	1676.3333	DCCM-1676-4	0.13274	0.00727	0.00268	0.01967	0.00077	0.00512
143	1676.6667	DCCM-1676-8	0.13849	0.00661	0.00176	0.01972	0.00055	0.00442
143	1677	DCCM-1677	0.13228	0.01350	0.00704	0.01831	0.00877	0.00429
143	1677.3333	DCCM-1677-4	0.26826	0.01076	0.00455	0.01752	0.00102	0.00498
143	1677.6667	DCCM-1677-8	0.04217	0.00228	0.00084	0.01855	0.00153	0.00114
143	1678	DCCM-1678	0.05659	0.00179	0.00062	0.00591	0.00000	0.00000
143	1678.3333	DCCM-1678-4	0.00540	0.00163	0.00092	0.00546	0.00000	0.00007
143	1678.6667	DCCM-1678-8	0.00000	0.00245	0.00064	0.00565	0.00000	0.00000
143	1679	DCCM-1679	0.02955	0.00234	0.00055	0.00551	0.00000	0.00018
143	1679.3333	DCCM-1679-4	0.00785	0.00231	0.00056	0.00564	0.00000	0.00008
143	1679.6667	DCCM-1679-8	0.00000	0.00184	0.00063	0.00573	0.00000	0.00000
143	1680	DCCM-1680	0.00000	0.00142	0.00061	0.00536	0.00000	0.00000
143	1680.3333	DCCM-1680-4	0.04737	0.00222	0.00061	0.00518	0.00000	0.00000
143	1680.6667	DCCM-1680-8	0.00000	0.00096	0.00041	0.00525	0.00000	0.00002
143	1681	DCCM-1681	0.04506	0.00062	0.00059	0.00605	0.00000	0.00024
143	1681.3333	DCCM-1681-4	0.00000	0.00195	0.00101	0.00627	0.00000	0.00081
143	1681.6667	DCCM-1681-8	0.00000	0.00078	0.00126	0.00507	0.00000	0.00049
143	1682	DCCM-1682	0.00000	0.00102	0.00138	0.00453	0.00000	0.00038
143	1682.3333	DCCM-1682-4	0.00000	0.00040	0.00086	0.00437	0.00000	0.00082
143	1682.6667	DCCM-1682-8	0.00000	0.00080	0.00131	0.00482	0.00000	0.00082
143	1683	DCCM-1683	0.00000	0.00258	0.00125	0.01046	0.00037	0.00023

Appendix B - Clay Fraction XRD Procedure

XRD Lab – Clay fraction preparation for XRD analysis

This procedure is inspired from the procedure established by Kübler in the XRD lab at university of Neuchâtel. XRD analysis of clay fraction requires to separate 2 size fractions: 2-16 µm and <2µm (supposed authigenic). This is a common procedure adopted in most of XRD lab worldwide.

Before starting separation, it is important to gently crush rock samples. Do not powder it too fine because it will destroy the clay texture and crystallinity. We advise to gently crush samples using agate mortar until obtaining a gravel to sand size.

Step 1: decarbonation

For this step you'll need the following:

- Boiling flask;
- A batch of 10% HCl (200 ml per sample). Mix 240 ml of 37% HCl with 760 ml of distilled water;
- 400 ml centrifuge bottles;
- Magnetic or glass stirrer ;
- Balance (digital scale);

This step must be conducted under fume-hood;

1. Add about 3 tablespoon of the crushed sample in boiling flasks;
2. Start the timer for 20 min;
3. Fill each boiling flask with 100 ml of HCl;

4. Stir periodically to ensure that the acid and sample thoroughly interact;
5. After 10 min pour another 100 ml in each flask;
6. Continue to stir;
7. After 20 min pour the supernatant liquid (acid solution + suspended particles) in the 400 ml centrifuge bottles. The solid left over can be disposed. Rinse the flasks just after. We don't want mud to dry;
8. Weigh each centrifuge bottles and adjust weight of each bottle with distilled water if necessary (the centrifuge won't run if a weight difference > 1 g between samples);

Step 2: acid wash

Once decarbonation completed, it is important to wash the sample until they reach a pH = 7. If we neglect this part, clays will continue to react with acid, changing composition, texture and polytype. The acid may also be released in the XRD machine during analysis, damaging the instrument with time.

1. Place each centrifuge bottles in centrifuge holder and run for 10 min at 5000 rpm;
2. After completion, dispose the supernatant acid in disposal drain, fill each bottle with 100 ml of distilled water. Close the lids (wash after each usage) and shake actively to dislodge sediment plated to the bottom; add another 100 ml and then centrifuge at 5000 rpm for 10 min (do not forget to weigh the samples to make sure the centrifuge is balanced);

3. Repeat step 2 until the solution starts to be cloudy. This is a sign of clay flocculation when the pH is ~7. This generally takes between 2 and 8 wash cycles (it depends on the sample's composition);
4. During the waiting time you can label 2x4 glass-slides as follow: SAMPLE# 2 and SAMPLE# 2-16. Also prepare 3 vials for each sample as follows: SAMPLE# Total, SAMPLE# 2-16 and SAMPLE# <2;
5. Once the supernatant liquid starts to be cloudy, dispose the water and add 1/3 of the bottle with distilled water. Shake vigorously to dislodge sediment plated to the bottle walls. Pour the solution in the vial SAMPLE# Total, and in 50 ml centrifuge tubes up to upper reference line (45 ml);

Step 3: Organic material removal (optional)

You only need to make this step if you are working with soil samples.

1. Add 50 ml of a 3% hydrogen peroxide solution to each sample and stir;
2. After effervescence slowed, add another 50mL of the peroxide solution to each sample and allow to sit until all effervescence stopped, ~4 hours.
3. The suspension is washed another 3 times at 5000 rpm for 10 min (same procedure than step 2);

Step 4: <2µm clay size separation

1. Set-up the centrifuge for 58 seconds at 1000 rpm;

2. Vigorously shake each tube (use lids for this, but be sure to use the same lids each time to avoid cross contamination), quickly place tubes in the centrifuge holder and run the centrifuge;
3. After the first run, collect the clay fraction using syringe until the solution reaches the lower reference line (35 ml). Drop sample onto the appropriate glass slide using pipette, pour the rest in the vial SAMPLE# <2;

4. Use distilled water to fill the 50 ml tubes back up to the upper reference line, then repeat step 1 - 3 more times to ensure you collected enough sample. In each time collect the solution up to the reference line and dispose it to ensure no <2µm fraction is remaining;

Step 5: 2-16µm clay size separation

1. This step doesn't involve centrifugation, the 2-16 µm fraction will be separated by gravity.
2. Set a timer for 97 seconds;
3. Fill the centrifuged tubes to the upper reference line (45 ml) with distilled water. Put the sample lid on, then vigorously shake the tube. Start the timer when you put down the tube in the tray;
4. Once the timer is up, collect the clay fraction using syringe up to the lower reference line (35 ml). Drop sample onto the appropriate glass slide using pipette, pour the rest in the vial SAMPLE# 2 - 16;

5. Be sure to rinse the syringe between each sample. To do so, fill 2 large beakers filled with distilled water. I fill the syringe with one of them and dispose the water in the sink; and then deeply clean with the second beaker;

Step 6: Let both clay fractions dry on the glass slides.

Once dry, as long as you can see the clay on the glass (cloudy) you should have enough sample. If you believe you don't have enough material, use the clay solution stored in the vials (be sure to shake it) and use a pipette to put a few drops on the glass slide, and let it dry again. Repeat this step until you believe there is enough sample for testing.

You can make a glycol treatment after analyzing them first. Alternatively, you can use the content of the vials to pour on other glass slide for special treatments;

Step 7: Ethylene Glycol treatment

This step is used to test for swelling clays (e.g. smectite). You can find detailed information in Poppe et al (2002) [A Laboratory Manual for X-Ray Powder Diffraction].

For this step you'll need the following: - Ethylene glycol; - Oven; - desiccator;

1. . Pour ethylene glycol to a depth of about 1 cm in the base of the desiccator;
2. Place the clay fraction slides directly on the desiccator shelf;
3. Place the desiccator in the oven at 70˚C overnight. Do not remove the mounts from the oven until right before they are going to analyzed;

Appendix C - Complete Sedimentary Log

A more complete version of Figure 4.1 has been added as a supplemental file.